Enhanced cell viscosity as a marker of premature senescence induced by lamin A/C alterations

Cécile Jebane[a], Alice-Anaïs Varlet[b], Marc Karnat[c], Lucero M. Hernandez-Cedillo[a], Amélie Lecchi[d], Frédéric Bedu[d], Camille Desgrouas[b], Corinne Vigouroux[e], Marie-Christine Vantyghem[f], Annie Viallat[a], Jean-François Rupprecht[c], Emmanuèle Helfer[a,*], and Catherine Badens[b,g,*]

[a]Aix Marseille Univ, CNRS, CINAM, Turing Centre for Living Systems, Marseille, France; [b]Aix Marseille Univ, INSERM, MMG, Marseille, France; [c]Aix Marseille Univ, Université de Toulon, CNRS, CPT, Turing Centre for Living Systems, Marseille, France; [d]Aix Marseille Univ, CNRS, CINAM, Marseille, France; [e]Assistance Publique–Hôpitaux de Paris (AP-HP), Hôpital Saint-Antoine, Centre de Référence des Pathologies Rares de l'Insulino-Sécrétion et de l'Insulino-Sensibilité (PRISIS), Service d'Endocrinologie, Paris, France, and Sorbonne Université, Centre de Recherche Saint-Antoine, Inserm UMR S938, Paris, France; [f]CHU de Lille, Endocrinology, Diabetology and Metabolism, Université de Lille, Inserm, UMR 1190, Translational research in diabetes, European Genomic Institute for Diabetes (EGID), Lille, France; [g]Laboratoire de Génétique Moléculaire, APHM, CHU de la Timone, Marseille, France

This manuscript was compiled on July 18, 2022

Lamin A/C is a crucial player in nuclear properties and its alterations cause different diseases sharing some cellular features such as misshapen nuclei or premature senescence. If the impact of lamin A/C alterations is well described at the molecular and nuclear scales, notably on nuclear mechanics, their effects on cells and tissues need to be clarified. Here, we used a microfluidic device to force cells into constrictions and infer their mechanical properties. We benchmarked the mechanical response of whole cells and isolated nuclei from a healthy individual to that of prematurely senescent cells (i) affected by the lamin A/C R482W mutation associated to type-2 familial partial lipodystrophy (FPLD2), or (ii) treated by a protease inhibitor which alters lamin A/C production. We further challenged the cells with cytoskeletal drugs to destabilize the actin and microtubule networks. We found that senescent cells are more viscous than non-senescent ones, and that this change is not explained solely by mechanical changes in nuclei. Rather, we showed a major contribution from the cytoskeleton and uncovered an unexpected role of microtubules in prematurely senescent cells. These results suggest that lamin A/C not only impacts the nucleus but also its interplay with the cytoskeleton. By unveiling the enhanced cell viscosity as a marker of premature senescence, our study on cell mechanical properties paves the way towards a fast method for characterizing laminopathy-affected cells and testing drug therapy response.

laminopathies | premature senescence | microfluidics | viscoelastic properties | lamin-cytoskeleton link

Lamin A/C, an intermediate filament underlying the nuclear envelope (NE), is a well-established key contributor to nuclear mechanical stability, shape, and rigidity (1–6). Diseases associated with mutations that alter lamin A/C, referred to as laminopathies, are characterized by diverse cellular features like abnormal nuclear shape and premature senescence (corresponding to cell aging) (7–13). Laminopathies are clinically heterogeneous and can be tissue-specific, like cardiomyopathies, or multi-systemic, like Hutchinson-Gilford progeria syndrome (HGPS, referred to as Progeria in this study) (14, 15). Among multi-systemic laminopathies, the type 2 familial partial lipodystrophy (FPLD2) predominantly affects adipose tissue, which results in dyslipidemia, a precocious type II diabetes, and an increased risk for cardiovascular diseases. The link between laminopathy severity, lamin A/C mutations, and the alterations of mechanical properties from the nuclear scale to the whole cell scale is still unclear (5, 12). A better understanding of the mechanisms at play will permit the precise characterization of new lamin A/C mutants and potentially the identification of novel therapeutical targets. So far, the few existing studies have mostly focused on nuclear mechanics, disregarding the changes that can occur at the cellular/tissue scale, and even these studies have no clear consensus. For example, in the case of the extensively studied Progeria, while there is a general agreement on a stiffer NE, the nuclear interior was measured to be either unaltered or softened (16, 17). In the case of cardiomyopathy, a decrease of both viscosity and elastic modulus of the nucleus was observed (18). Artificial lamin A/C depletion in mouse embryonic fibroblasts led to a similar decrease of nuclear viscosity and elastic modulus (18, 19). Therefore, the exact mechanical changes in the nucleus due to lamin A/C alterations are not completely understood yet, and, notably, the consequences at the cellular level are still unknown.

Here, we use the microfluidic technique, widely employed to measure mechanical properties of cells (20–24), to investigate the impact of two types of lamin A/C alterations at the nuclear and cellular levels. The microfluidic device allows us to apply compression stress on cells over a short time of a few seconds, thus avoiding reorganization of cellular components, and therefore to probe the cellular intrinsic properties. Microfluidic measurements are combined with a semi-automated image analysis and a rheological model to extract the cells' viscoelastic properties from their deformation. We provide a quantitative data set on mechanical properties of human skin fibroblasts with alterations induced by an FPLD2-associated mutation or an *in vitro* treatment with a protease inhibitor (Atazanavir) known to induce premature senescence phenotypes. Our results show that the main mechanical feature of cells displaying premature senescence, whether induced *in vitro* or by the mutation, is an increase of cell effective viscosity.

Results

AZN treatment drives a premature senescence phenotype in fibroblasts similar to that induced by lamin A/C R482W mutation. Two different primary cell models were selected to study cell viscoelastic properties in premature senescent condition:

1) fibroblasts issued from a healthy individual and treated with Atazanavir (AZN), a drug which alters lamin A/C maturation and production (8, 9, 11); and 2) fibroblasts issued from two patients with FLPD2 carrying the canonical lamin A/C R482W mutation in heterozygous condition (patients 8 and 12 from Ref. (25)).

As a phenotype of premature senescence induced by AZN treatment has been demonstrated in endothelial cells only (8, 9, 11), we first characterized the response of control healthy fibroblasts to AZN on morphological, proliferation, and senescent markers, in order to confirm their sensitivity to AZN and to select an optimal concentration. Cells were treated for 48 h with increasing concentrations of AZN, or incubated only with its solvent, DMSO, as a control. High levels of nuclear aberrations were observed, similar to those observed in cells from patients with FPLD2 or from a patient with Progeria carrying the lamin A/C G608G mutation (Fig. 1A-C). The impact of increasing AZN concentration was also confirmed on proliferation capacity by measuring Bromodeoxyuridine incorporation, and on senescence level by estimating the cellular SA-β-galactosidase activity (Fig. 1D-E). From these data the concentration of 50 µM was chosen as a compromise to efficiently drive senescence while being non toxic for the cells.

As a second step, we evaluated the impact of AZN treatment regarding cellular and nuclear volumes, and compared it to the impact of the FPLD2-associated mutation (Fig. S1). Indeed, it was crucial to verify that the volumes of cells or nuclei are comparable between cell types in order to discard any size effect that can impact the cell behavior in the microfluidic experiment. Second, knowing the volumes of cells and nuclei was also required to engineer the microfluidic device described hereafter. Volumes were derived from confocal imaging of cells in suspension, to mimic the microfluidic configuration. Cellular and nuclear volumes of control fibroblasts treated with AZN increased by 37% and 13%, respectively, with respect to those of DMSO-incubated fibroblasts. It is of importance to compare AZN treatment effect to that of DMSO incubation as the latter affects both volumes (around 15% of relative change). Volumes of fibroblasts from the patients with FPLD2 (referred to as K and M) were compared to those of control untreated cells and to those of fibroblasts from a patient with Progeria, used as a positive control of volume increase. As expected, both cellular and nuclear volumes of Progeria cells are much larger than those of untreated cells (26, 27). In contrast, the volumes of FPLD2 cells and nuclei remain closer to those of untreated cells (< 20% relative change).

Altogether, senescence assays (Fig. 1) and volume quantification (Fig. S1) suggest that AZN treatment induces premature senescence in control fibroblasts, with a phenotype similar to that induced by the FPLD2 mutation. As their volumes are close, AZN, FPLD2, and control cells can be compared in microfluidic experiments, but not Progeria cells which are too large.

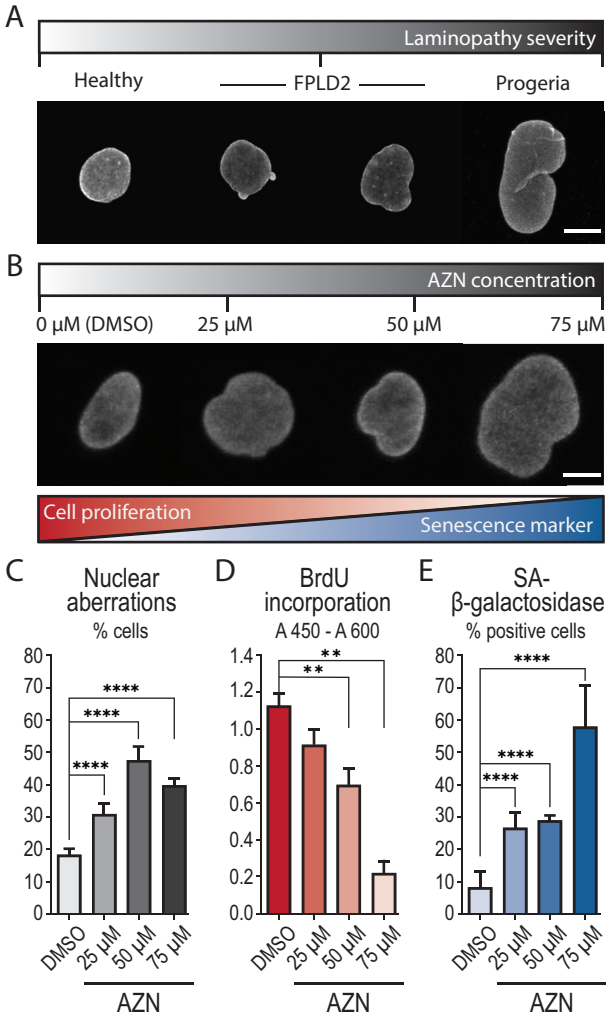

Fig. 1. Atazanavir (AZN) treatment induces cellular phenotypes associated with premature senescence. Control fibroblasts were treated for 48 h with increasing doses of AZN or incubated with DMSO as a control. (A-B) Representative images of nuclear aberrations (abnormal size or shape) observed in (A) healthy fibroblasts or fibroblasts from patients with FPLD2 carrying the lamin A/C R482W mutation, or from a patient with Progeria, and (B) control fibroblasts treated with AZN. Nuclear envelope is stained using a lamin A/C specific antibody. Scale bars: 10 µm. (C) Percentage of cells displaying nuclear aberrations. (D) Bromodeoxyuridine (BrdU) incorporation reporting cell proliferation ability. (E) Percentage of SA-β-galactosidase positive cells identified as senescent. Errors are standard deviations. Number of experiments: N ≥ 3 (C-E); number of analyzed cells: $n \geq 1000$ (C) and ≥ 500 (E).

A two-height microfluidic device to assay the cell response to mechanical constraint. As lamin A/C participates in nucleus mechanics and connects to the cell cytoskeleton (28, 29), premature senescence induced by AZN treatment or lamin A/C mutation is expected to alter the whole cell response to mechanical stress. To investigate the cell mechanical properties, we designed and fabricated a microfluidic device consisting of a wide channel with parallel constrictions to constrain the cells (Fig. 2A-B). An original feature of the device lies in the two heights along the channel (Fig. 2B): the device contains the constriction region of low height in the center, and, to avoid excessive pre-stress, a higher zone 200 µm away from both ends of this region. Cells are thus strongly confined in height only 200 µm before reaching the constrictions, adopting a "pancake" shape, and experience an additional lateral confinement when entering the constrictions. The constrictions of 6×6 µm^2 square cross-section are small enough to squeeze both the cells and their nuclei. Consequently, the nuclei are expected to contribute to the cell behavior. The device allows to observe the passage of tens of cells through the constrictions and, therefore, to analyse the cell behavior with high statistics. When pushed through constrictions, under controlled pressure drop, all cell types display a typical deformation dynamics,

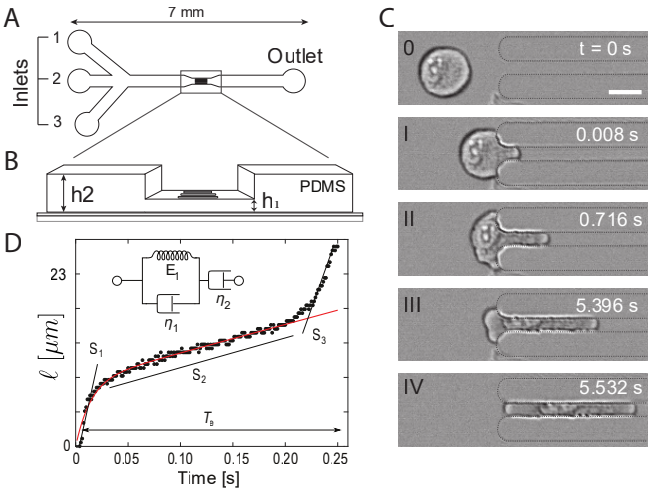

Fig. 2. Microfluidic device, typical experiment, data processing and analysis. (A) Top-view schematics of the microfluidic device. Inlets (1) and (3) are used for injecting buffer solutions while cells are injected through inlet (2). Controlled pressure drop is applied between inlets and oulet to push cells through constrictions. (B) Zoomed 3D-view of the constriction zone, with two different heights: h_2 for the main 300-µm wide channel and h_1 for the constrictions (length l, width w). l = 100 µm, $w = h_1$ = 6 µm, h_2 = 10 µm. The low-height region is 500 µm long in total, including the constrictions. (C) Timelapse of a 24-µm cell entering a constriction of width w. Scale bar: 15 µm. (D) Typical time evolution of the cell tongue length $\ell(t)$. The curve is analyzed using two methods: i) It is decomposed into three linear parts, of slopes S_1 to S_3, which correspond to the cell entry time T_e; ii) The first two parts of the curve are fitted (in red) using a rheological model which combines a Kelvin–Voigt solid (a spring of constant E_1 in parallel with a dashpot of viscosity η_1) in series with a dashpot of viscosity η_2 (see inset).

with five distinct successive phases, named 0 to IV (Fig. 2C and Movie S1). From movies of cell passage, the length of the cell portion in the constriction (named cell tongue hereafter) is tracked (Fig. 2D, and Movie S2). The cell entry is composed of phases I-III, corresponding to three regimes with different dynamics of cell tongue elongation. Once the cell has fully entered inside the constriction, its deformation is maximum and it transits rapidly through the constriction, corresponding to phase IV.

Cells under AZN treatment or carrying the lamin A/C R482W mutation display an increase in viscosity. Using our microfluidic device, we measured the time evolution of the tongue length ℓ(t) as cells entered in and transited through constrictions. The curves were analyzed using two approaches (Fig. 2D): (i) we considered the entry time and the slopes of the three entry regimes approximated as linear; and (ii) we fitted the two first regimes using a rheological model (inset in Fig. 2D). We compared control fibroblasts either untreated (UNT), incubated with DMSO (DMSO) or treated with AZN (AZN), and fibroblasts from the patients with FPLD2 (M,K). As major clinical signs of FPLD2 are dyslipidemia and type II diabetes, we also used fibroblasts from a diabetic patient with the same symptoms but without lamin A/C alteration (patient 17 from Ref. (30), named T2D hereafter) to validate that our assay specifically discriminates laminopathic cells.

Entry time and linear regimes as a first analysis. We first analyzed the cell global behavior by considering their entry time in constrictions, T_e (Figs. 3A and S3A). AZN, M and K cells enter within 1.4, 1.7 and 3 s, respectively. They are at least 3 times slower than UNT and DMSO cells which enter within approximately the same time (0.4 and 0.46 s), confirming that DLSO, the AZN solvent, has no effect on T_e. Additionally, T2D cells, though slower than UNT cells (0.54 s), enter much faster than FPLD2 or AZN-treated cells, suggesting that the strong slowdown is specifically related to lamin A/C alterations. Upon sorting cells by volume, entry times shift to higher values as cellular volumes increase, as expected. However, at comparable volumes, FPLD2 and AZN cells are systematically slower than UNT and DMSO cells, respectively (Fig. S3B). Thus, the observed slowdown of the entry is due to mechanical changes induced by lamin A/C alterations in the senescent cells and not to a size effect.

Next, we deciphered the dynamics of the entry regimes, considered as linear, by measuring their slopes $S_1 - S_3$ (Fig. S3). As the second regime was much slower than the two others, it was hypothesized to correspond to the entry of the large and stiff nucleus. The three regimes are actually affected, in a similar way to the entry time: in comparison with UNT and DMSO cells, both AZN treatment and FPLD2-associated mutation decrease all slope values, meaning that they slow down all regimes. In contrast, T2D cells show no difference when compared to UNT cells, except an increase in S_3, confirming a different mechanism for cellular alterations. As all regimes are affected, i.e. the entry of the nucleus and of every other part of the cell, this questions how lamin A/C alterations impact the whole cell structure.

The Jeffreys rheological model as a second analysis. We used a rheological model to further analyze the cell dynamics and extract their viscoelastic properties (Fig. 3). Here, the Laplace pressure ΔP_c is relatively small as compared to the applied pressure drop ΔP, which implies that the applied stress is relatively constant throughout the compression experiment. The Laplace pressure is the critical pressure required to push cells through constrictions and relates to the cell cortical tension γ (see SI for details). By measuring the pressure drop at which cells starts to flow through constrictions, we estimated an upper limit of ΔP_c around 2 kPa, which is indeed well below the applied pressure drop ΔP of 16.5 kPa. This corresponds to a cortical tension of a few 10^{-3} N.m^{-1}, consistent with the literature (31–33). Assuming a constant applied stress on the cell and volume conservation, the cellular deformation, i.e. the cell tongue length, is compatible with the Jeffreys model, which consists of a Kelvin-Voigt solid (a spring of constant E_1 in parallel with a dashpot of viscosity η_1) in series with a dashpot of viscosity η_2 (Fig. 2D, inset; see SI for details). Following the method presented in Refs. (18, 34), the time evolution of the cell tongue then reads as:

$$\ell(t) = \frac{R_{\text{eff}}\Delta P}{E}\left(1 - e^{-\frac{E}{3\pi\eta_1}t}\right) + \frac{R_{\text{eff}}\Delta P}{3\pi\eta_2}t, \qquad [1]$$

where R_{eff} is the effective radius of the constriction and $E = E_1/\pi R_{\text{eff}}$ is an effective elastic modulus. At small deformations and short-time scale, a viscoelastic regime dominates with a characteristic viscoelastic time τ which relates to the effective elastic modulus E and to a short-time viscosity η_1 as $\tau = 3\pi\eta_1/E$. At larger deformations and long-time scale, a linear viscous regime dominates with a long-time viscosity η_2.

The $\ell(t)$ curves of individual cells were fitted using Eq. (1) to derive their intensive viscoelastic properties: Figure 3B-C displays the median fits for UNT *vs* M/K cells, and for DMSO *vs* AZN cells, respectively. At long-time scale (i.e., in the linear viscous regime), the fits of FPLD2 and AZN cells clearly

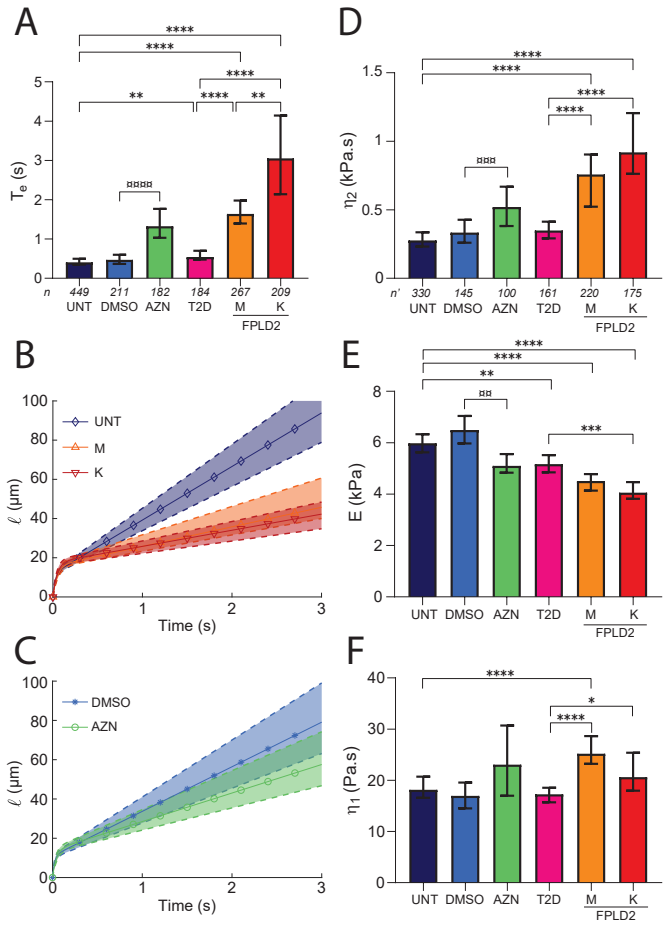

Fig. 3. AZN treatment and lamin A/C R482W mutation alter cell rheological behavior. UNT: untreated control cells (control); DMSO: control cells incubated with DMSO (AZN control); AZN: control cells treated with AZN; T2D: cells from diabetic patient; M,K: cells from patients with FPLD2 carrying the R482W mutation. (A) Entry time in 6×6-μm^2 constrictions T_e (median ± 95% CI). (B-C) Fits of tongue length ℓ as a function of time t ($t = 0$ defined at cell contact with constriction), for (B) UNT, M and K cells, and (C) DMSO and AZN cells. Solid curves with symbols indicate the median fits; dashed upper and lower curves delineate the 95% CIs; the curves are plotted using parameter values from Table 1 in Eq. (1). (D-F) Fit-extracted rheological parameters: long-time viscosity η_2 (D), short-time effective elastic modulus E (E) and viscosity η_1 (F). Medians ± 95% CIs are displayed. Significant differences: AZN *vs* DMSO cells (¤), FPLD2 and T2D *vs* UNT cells (*). Number of experiments: N ≥ 3; *n*: number of analyzed cells (A); *n'*: number of fitted curves (D,E,F).

	UNT	DMSO	AZN	T2D	M	K
τ (ms)	30 [25-34]	24 [20-28]	43 [33-49]	30 [28-34]	51 [45-59]	49 [41-54]
E (kPa)	6.0 [5.6-6.3]	6.5 [6.0-7.0]	5.1 [4.8-5.6]	5.2 [4.8-5.5]	4.5 [4.1-4.8]	4.1 [3.8-4.5]
η_1 (Pa.s)	18 [17-21]	17 [15-20]	23 [16.6-31]	17 [16-19]	25 [23-29]	21 [18-25]
η_2 (Pa.s)	277 [232-336]	333 [260-428]	521 [381-668]	349 [292-413]	758 [522-904]	920 [762-1206]

Table 1. Rheological parameters (Median [95% CI]). Significant differences: AZN *vs* DMSO cells, ns * ** * ****; T2D/M/K *vs* UNT cells, ns * ** *** ****.**

diverge from those of their respective controls (whose fits are similar, Fig. S4A). On the contrary, the fit of T2D cells is similar to that of UNT cells (Fig. S4B). The long-time viscosity η_2 is extracted from the linear part of the fit as the slope relates to η_2 as $R_{\text{eff}}\Delta P/3\pi\eta_2$ (Fig. 3D). While UNT/DMSO and T2D cells have a comparable viscosity, of the order of 300 Pa.s, AZN and FPLD2 cells display a higher viscosity, by at least 50%. At short-time scale, the characteristic viscoelastic time τ and the effective elastic modulus E (Fig. 3E) are extracted from the fits, and the short-time viscosity η_1 is derived (Fig. 3F). The elastic modulus E is affected in AZN and FPLD2 cells, lower by 22 to 32% compared to that of DMSO and UNT cells. Cells from the T2D patient also display a slightly lower modulus. The viscoelastic time τ is similar for UNT, DMSO and T2D cells while it is larger for senescent cells. The short-time viscosity η_1, which varies as τE, is roughly similar for all cell types (senescent cells display a trend towards larger η_1 values, which is significant only for M cells). All rheological parameters are summarized in Table 1 (corresponding dotplots in Fig. S5).

We noted that the short-time viscosity η_1, around 20 Pa.s in all cell types, is well below viscosities reported for whole cells, which range between 10^3 and 10^4 Pa.s (2, 18). However, the values are consistent with lower range values of cytoplasmic viscosity which span from 1 to 10^4 Pa.s (18, 35, 36). Thus, we hypothesized that, at short-time scale, we probe the viscosity of a bleb. Cells were stopped at different timepoints of entry/passage in constrictions, and imaged together with actin and nucleus (Fig. S6). As soon as cells contact the constrictions, blebs are observed at their front, in line with our hypothesis.

Taken altogether, our data highlight that lamin A/C alterations, induced by either AZN treatment or FPLD2-associated R482W mutation, give rise to a higher long-time viscosity and a lower effective elastic modulus. The short-time viscosity, however, is barely affected as it relates to a bleb which forms at the front of the cells when it contacts the constriction, a process that is expected not to depend on the nucleus. The T2D cells from the diabetic patient respond differently than the FPLD2 cells: while they display a decreased elastic modulus, like FPLD2 cells, their viscosity is similar to that of control cells. Thus, the increased viscosity is likely a marker of lamin A/C alterations, which can be assessed with our microfluidic setup.

The whole cell response to mechanical constraint does not depend exclusively on the nucleus. So far, the observed behavior corresponded to the whole cell response, with combined contributions of both the nucleus and the cytoplasmic content. The similar trends of entry time T_e and viscosity η_2 extracted from the long-time viscous regime suggested that T_e is dominated by η_2 (Fig. 3A, D). As we attributed this regime to the nucleus, we decided to investigate the intrinsic properties of isolated nuclei in order to assess whether the cell slowdown was related to changes in nuclear viscosity. Similar microfluidic experiments, albeit with smaller 3×3-μm^2 constrictions, were performed on nuclei extracted from UNT, DMSO, AZN and both FPLD2 cells, and the nucleus tongue length was computed.

Isolated nuclei display a behavior identical to that of cells (Figs. 4A and 2C, Movie S3), with three entry phases. However, the nucleus entry in constriction is much faster, within

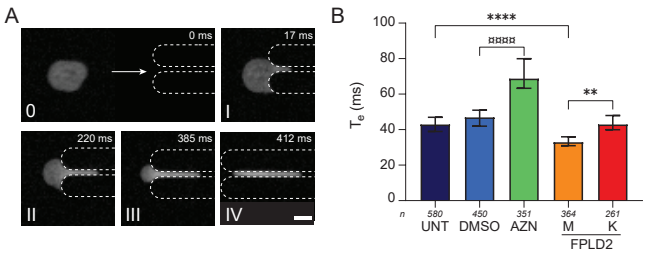

Fig. 4. Nucleus behavior as a function of cell type differs from cell behavior. (A) Timelapse of a 20-µm nucleus entering (I-III) and transiting (IV) through a 3×3 μm^2 constriction. Nucleus is labeled with Hoechst. Scale bar: 10 µm. (B) Entry time of isolated nuclei in constrictions T_e (median ± 95% CI). Nuclei from UNT: untreated control cells (control); DMSO: control cells incubated with AZN solvent (AZN control); AZN: control cells treated with AZN; M,K: cells from patients with FPLD2. Number of experiments: N ≥ 4; *n*: number of analyzed nuclei.

a few hundreds of ms, and the three entry regimes of the tongue length are not always distinguishable. Hence, only the entry time T_e is extracted from the tongue length curve (Fig. 4B). In accordance with the trend observed in whole cells, AZN treatment increases the entry time of the nuclei by approximately 50% compared to incubation with DMSO, regardless of the nuclear size (Fig. S7A-B). Strikingly, in contrast with the strong slowdowns observed in intact cells, M and K nuclei enter as fast as UNT ones, or even faster, especially in the largest volume range (Fig. S7C). Altogether, the results suggest that our observations on isolated nuclei are linked to changes in nuclear properties and not to a size effect, and that the nuclei affected by the R482W mutation may respond differently to mechanical stress.

Assuming the entry time of isolated nuclei is dominated by their viscosity, like whole cells, the observed entry times show that AZN treatment increases the nuclear viscosity while the lamin A/C R482W mutation decreases it, notably in FPLD2 M nuclei. These different effects can be explained by the fact that AZN treatment impacts the lamin A/C maturation only whereas the FPLD2-associated mutation produces in addition an abnormal lamin A/C. In both conditions, our results show that the behavior of isolated nuclei does not reproduce that of whole cells, suggesting that the cell response to mechanical constrain does not exclusively depend on the nuclear envelope, but rather on its interplay with other cell components, such as the cytoskeleton.

Microtubule network is involved in senescent cell response to mechanical constraint. Among the cytoskeletal components, actin filaments and microtubules are known to participate in cell stability and resistance to mechanical stress, and are connected to the lamin A/C meshwork (28, 29, 37). To assess their contribution to cell response, actin and microtubule networks were destabilized individually or together, using cytoskeletal drugs, in UNT, AZN and FPLD2 K cells (Figs. 5A-B and S8). We chose cells from patient K as they displayed the strongest change in η_2 viscosity compared to UNT cells (see Fig. 3 and Table 1). Drug treatments were compared to control condition defined as incubation with the drug solvent, DMSO. Just as for cells with intact cytoskeleton, the entry time T_e and viscoelastic parameters (E, η_1, and η_2) were quantified (Fig. 5C-N and Table S1).

Cytoskeletal drugs induce significant changes when compared to DMSO condition. Globally, for the three cell types,

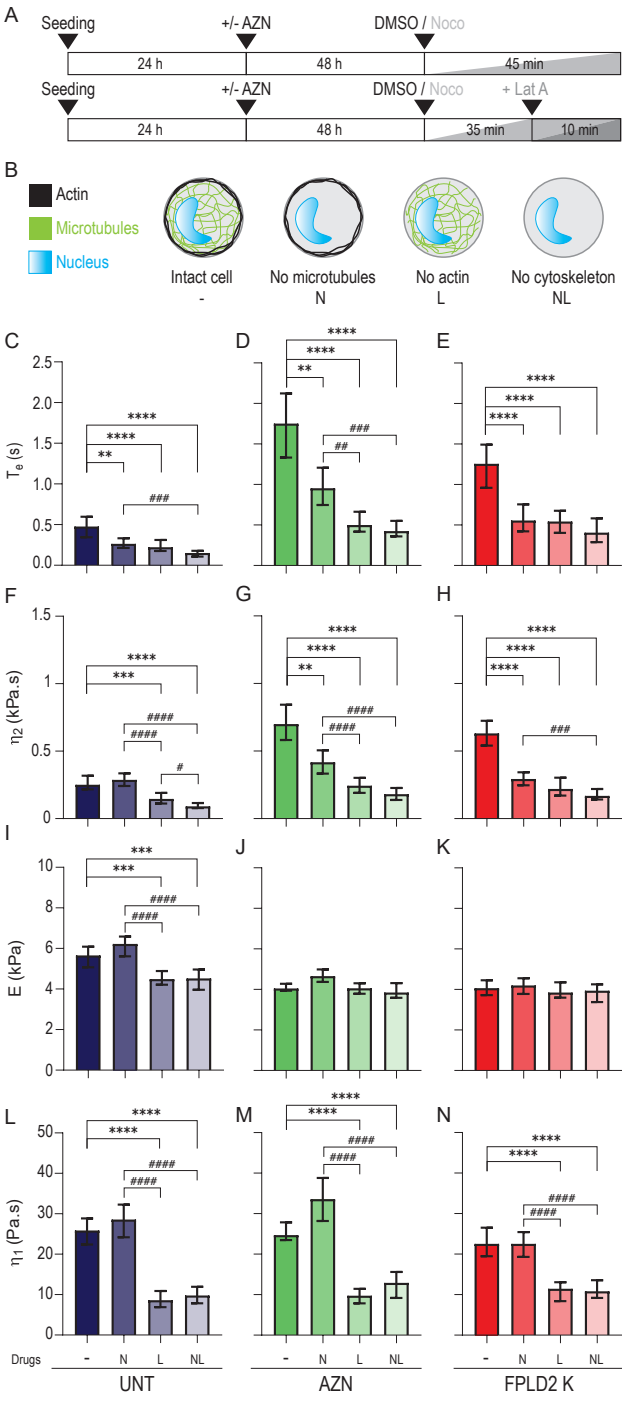

Fig. 5. Actin filament and microtubule destabilization accelerates cell entry into constrictions and decreases long-time viscosity in senescent cells. (A) Timeline protocol for cytoskeletal drug treatments: 72 h after seeding, cells, treated or not with AZN, are treated with nocodazole (45 min), latrunculin A (10 min), or both (35 min with nocodazole, then 10 min with both drugs). (B) Sketched effect of drug treatments on cells, with nocodazole, N (resp. latrunculin A, L) leading to microtubule (resp. actin) destabilization. Control condition is incubation with drug solvent, DMSO. (C-E) Entry time in constrictions T_e and (F-N) fit-extracted rheological parameters of untreated control cells (UNT, dark blue), AZN-treated cells (AZN, green), and FPLD2 cells (FPLD2 K, red) upon drug treatments. Medians ± 95% CIs are displayed. Significant differences: drug treatments *vs* DMSO control (*), and between drug treatments ($^{\#}$). Number of experiments: N ≥ 3; number of analyzed cells: *n* ≥ 100 (C-E); number of fitted curves: *n'* ≥ 60 (F-N).

the destabilization of either microtubule or actin network induces an approximately 50-60% decrease in entry time T_e, and the disruption of both networks leads to a larger decrease of 70% (Fig. 5C-E). Regardless of treatment conditions, the trend is conserved, with senescent AZN and K cells always entering slower than non-senescent cells. While microtubule disruption decreases entry time T_e in the three cell types, it does not impact long-time viscosity η_2 in UNT cells, as expected from the literature (38, 39). However, it decreases η_2 by at least 40% in both AZN and K cells. Actin disruption, on the other hand, decreases η_2 in all cells, by 40 to 65%, suggesting a similar role of actin in the three cell types (Fig. 5C-E vs Fig. 5F-H). Thus, the actin network contributes to the long-time viscosity in both non-senescent and senescent cells, while the microtubule network is involved only in senescent cells. In contrast, the short-time viscosity η_1 is barely impacted by microtubule disruption while it is strongly affected by actin disruption, with at least a 50% decrease in all cells, indicating once again that actin acts independently of cell type (Fig. 5L-N). Strikingly, the effective elastic modulus E is not impacted in senescent cells, under any treatment condition, and UNT cells only display a 20% decrease upon actin disruption. This suggests that the E modulus measured here poorly relates to the actin cortex.

Our data show that the actin network has a major impact on long- and short-time viscosities, independently of the senescence state of the cells, and that the microtubule network has an additional impact on the long-time viscosity exclusively in senescent cells. The effect appears to be cumulative as removing both networks simultaneously induces an approximately 70% decrease in entry time and long-time viscosity, for both non-senescent and senescent cells. Altogether, our results suggest that the nucleus alone contributes, at most, by 30% to the viscous response of the whole cell, and that the major contribution is from the cytoskeleton in connection with the nucleus.

A simple scaling law to detect changes in long-time viscosity. The above analysis requires thorough tracking of the cell entry in the constriction and subsequent analysis of the cell tongue length to derive all rheological parameters. As entry time T_e and long-time viscosity η_2 behave similarly, we wondered whether we could define a simpler, faster method to screen the cell behavior and highlight alterations of the viscous behavior. With appropriate approximations, Eq. (1) can be simplified, leading to a scaling law between the entry time and the cell initial diameter: $T_e \propto L_0^2$ (see SI for details). This law was used to fit the $T_e(L_0)$ data sets and derive a factor ν: $T_e = \nu L_0^2$ (see, for example, the fits for UNT and K cells in Fig. S9A). The ν values from each cell type were normalized to that of UNT cells to illustrate the relative change. The ν ratios behave almost identically to the η_2 ratios ($\eta_2/\eta_{2\mathrm{UNT}}$) obtained with the precise fits of the tongue length curves (Fig. S9B). Thus, the measurement of the cell entry time T_e and its dependence to the cell initial size L_0 seems appropriate to perform a first rapid comparison of the long-time viscosities between different cell types. This validates this approach to get a rough estimation of viscosity differences, allowing a fast screening of cell populations to detect whether they are affected by premature senescence associated to lamin A/C alterations.

Discussion and conclusion

In the present study, we performed microfluidic experiments combined with theoretical methods to explore changes in cellular and nuclear mechanical properties in the context of lamin A/C-related senescence. We showed that premature senescence, caused either by AZN treatment or FPLD2-associated R482W mutation, correlates with an increase of cell viscosity which mainly depends on actin and, unexpectedly, on microtubules.

Cell mechanical properties have been investigated with various experimental approaches (micropipette, atomic force microscopy, microfluidics, etc.) and span over several orders of magnitude, depending on the technique and the explored timescale. Here, the values of the long-time viscosity η_2, all found in the kPa.s range, are within the lowest values reported in the literature (dispersed between 0.5 and 100 kPa.s (18, 40)). The effective elastic modulus E displays values around 5 kPa that are also consistent with the literature (1 to 15 kPa, measured on cell cortex or nuclei (41–43)). The opposite increase and decrease of η_2 and E observed here in senescent cells differ from the decrease of both viscosity and elastic modulus reported in studies on lamin A/C depleted systems, where viscoelastic fluid models were used as well (18, 19). Decreases of both parameters was also observed with dilated cardiomyopathy-associated K219T mutation (18). Only Progeria-affected cells showed an increased nuclear stiffness (16, 17), which corresponds to a higher elastic modulus and seems contradictory with the lower modulus measured with our system. However, in all these studies, the observation timescale is of the order of a few minutes and the imposed deformation is usually small, of the order of a few %. In contrast, we assessed here the dynamic response of cells at the second-timescale, for high stresses and deformations (16.5 kPa pressure drop, 6×6 μm^2 confinement). In such conditions, we probe the intrinsic properties of cells as the cellular components do not have time to reorganize under the applied stress.

We used the Jeffreys model to fit the time evolution of the cell tongue length and extract the cell rheological properties. With a cell viscosity η_2 around 500 Pa.s (Table 1), a flow rate V around 40 $\mu m.s^{-1}$, and a surface tension $\gamma = 10^{-3}$ $N.m^{-1}$, we estimate the capillary number $Ca = \eta_2 V/\gamma$ around 20 (44), which confirms that the long-time viscous dissipation dominates over surface tension forces. This validates our assumption that the Laplace pressure contribution to the stress applied on the cell can be neglected. We also applied a power-law fit to the curves as in Refs. (16, 18). This second common approach provides consistent results with the Jeffreys model (see model description and Fig. S10 in SI).

The pressure drop in our experiments is much higher than the critical pressure of roughly 1 kPa shown to disrupt the connection between the actin cortex and the cellular membrane (36). Consistently, we observed the formation of a bleb at the cell front, which does not retract through the entry process. In addition, the observed impact of actin destabilization on short-time viscosity η_1 comforts the fact that η_1 depends on actin and corresponds to the front bleb. Altogether, this led us to propose a model of the cell entry in constriction depicted in Fig. 6. How lamin A/C alterations may impact the blebbing process is still unknown and further studies are required to answer this question.

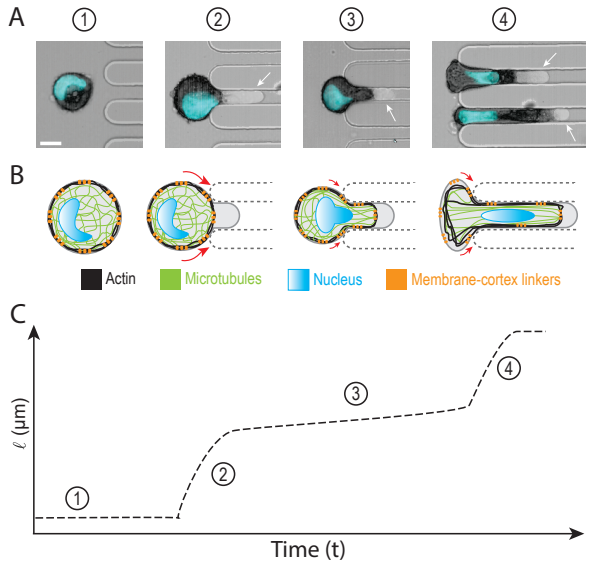

Fig. 6. Model of the cell entry in constriction. (A) Images of cells in brightfield, superimposed with F-actin (black) and chromatin (blue) in epifluorescence; arrows highlight blebs at the cell fronts. Scale bar: 10 µm. (B) Schematics of the cell and its components corresponding to images in (A). (C) Schematized curve of cell tongue length $\ell(t)$ with timepoints corresponding to (A-B): (1) the cell flows towards the constriction; (2) the cell contacts the constriction, membrane-cortex links break and a bleb forms at the cell front; (3) nucleus and cytoskeleton slowly deform to enter the constriction; (4) the major part of the cell has entered and the cell rear deforms rapidly, membrane-cortex links may rupture leading to an additional bleb at the cell rear.

In contrast with the common statement that microtubules have a minor contribution to the cell viscoelasticity (38, 39), we found that the microtubule network contributes to the viscous response of the senescent cells studied here, suggesting changes in microtubule organization and/or dynamics. Indeed, lamin A/C alterations, which directly impact the nuclear envelope, might affect the microtubule organization through the connection between the nuclear envelope and the cytoskeleton. This is in line with a work showing altered microtubule structure in rat cardiomyocytes carrying lamin A/C mutations (45). The dynamics of microtubules could also be affected as a recent study suggested that it decreases when cytoplasm viscosity increases (46). An alternative explanation relies on the known impact of microtubules on cell contractility and traction forces in adherent cells (47–49). Because we observed in our study an impact of microtubule depolymerization in senescent cells, it might indicate an altered basal level of cellular contractility.

We demonstrated that all dynamic regimes of the cell deformation are affected by lamin A/C alterations. In particular, the changes in the viscous regime are not reproduced with isolated nuclei. This suggests that the nucleus alone is not responsible for the observed changes and that its links with the cytoskeleton are essential to the cellular viscosity, especially through the linker of nucleoskeleton and cytoskeleton (LINC) complex, that connects the nuclear lamina to cytoskeletal elements and provides a structural link between the nucleus and the cytoplasm (50, 51). Deciphering the exact impact of the nucleus and its connection to the cytoskeleton on the cell tongue elongation regimes would require to detect the nuclear position in the cell, which is not doable in our current setup. Additionally, since the effective elastic modulus E is too high (approximately 5 kPa) to relate to the front bleb, and is independent of actin and microtubules, it might be related to other components of the cell such as the intermediate filament vimentin (52). Even though the significance of the E modulus is still not understood, our approach remains efficient to evidence differences in long-time viscosity.

To conclude, we developed a microfluidic test which unveils a mechanical signature of cells with lamin A/C alterations that is different from the one of healthy and diabetic cells, namely an increase of the long-time effective viscosity at the cellular level. We also uncovered an unexpected impact of microtubules in prematurely senescent cells. Further investigations should be conducted to assess the sensitivity of our test, for example by testing lamin A/C level modulation, like depletion or overexpression, or other pathogenic variants. Our mechanical test could provide a method for characterization of missense variants in lamin A/C and for drug therapy response evaluation in some laminopathies. Additionally, we showed that the long-time viscosity can be roughly estimated by the sole measurements of the entry time and initial cell diameter. This simple and rapid analysis could be used either to decide whether it is worth performing a rheological analysis for a fine study of cell properties, or, for a diagnosis purpose, to screen large cell populations and identify those which are senescent.

Materials and Methods

More details are available in SI.

Cells, treatments and senescence assays. *Cells.* Fibroblast cell lines are summarized in Table S2 (SI). Cells were cultured at 37°C under 5% CO_2 in low glucose Dulbecco Medium Eagle Modified (DMEM) supplemented with 15% fetal bovine serum (FBS) and 2 mM L-Glutamine (DMEM, FBS, L-Glutamine, Gibco). *Isolated nuclei.* Nuclei were extracted by cell lysis using a detergent-based method (53) right before microfluidic experiments. *Cell treatments.* Control cells were incubated with AZN during 48 h before performing senescence tests or microfluidic experiments. Cells were also treated with 200 nM latrunculin A (resp. 10 μM nocodazole) for 10 (resp. 45) min, or both, before microfluidic experiments (latrunculin A, nocodazole, Sigma-Aldrich). *Senescence tests.* Bromodeoxyuridine incorporation and SA-β-galactosidase activity were assessed following manufacturers' instructions (Roche Applied Science and Cell Signaling Technology, respectively).

Fluorescence microscopy. *Nuclear aberrations.* Lamin A/C immunofluorescence was performed on fixed adhered cells and nuclear aberrations were quantified as previously described (54). *Cellular and nuclear volumes.* Adhered cells were labeled for plasma membrane (Cell Brite, Biotum) and DNA (Hoechst, Invitrogen) using manufacturer and standard protocols, then resuspended and Z-stacks were acquired by confocal microscopy for membrane and DNA fluorescence signals. FIJI software was used to detect cell and nucleus contours, and compute their respective volumes.

Microfluidic device and experiments. Microfluidic chips were made of polydimethylsiloxane (PDMS, Dow Corning) using standard lithography technique of microfabrication. Cells were cultured for 72 h (including AZN treatment) before performing microfluidic experiments at 37°C on an inverted microscope (IX71, Olympus) equipped with a 20× objective and high-speed cameras (Mini UX, Photron and VEO310, Phantom). A flow controller (MFCS-8, Fluigent) was used to control the pressure drop between chip inlets and outlet, and the cells/nuclei flow in the constrictions. Cells (resp. isolated nuclei) were observed in brightfield (resp. epifluorescence) microscopy and movies were acquired at frame rates varying from 250 to 800 fps (resp. 500 to 1000 fps).

Image processing and analysis. Movies of cells were pre-processed using FIJI sofware to enhance contrast and segment the cells. Movies of isolated nuclei were processed differently via automatic tracking (FIJI) and segmentation (Matlab). Matlab software (MathWorks, r2018b version (55)) was used to fit a bounding box around the segmented cells/nuclei and measure their length. The elongation ratio was computed over time.

Data analysis. First, a Matlab home-made routine was used to determine the slopes of the three regimes and the entry time from the tongue length curve $\ell(t)$ curves. Second, the two first phases of the $\ell(t)$ curves were fitted using Matlab fit function based on the model equation to extract the rheological parameters. Fits were selected with $R^2 \geq 0.85$, leading to more than 50 analyzed cells per cell type.

Statistical analysis. Statistical calculations were performed using Prism 6.0 statistical software (GraphPad).

ACKNOWLEDGMENTS. The project leading to this publication has received funding from Excellence Initiative of Aix-Marseille University - A*MIDEX (A-M-AAP-ID-17-66-170301-11.30) and from France 2030, the French Government program managed by the French National Research Agency (ANR-16-CONV-0001).
CJ, AAV, and MK equally contributed to this work. EH and CB share last authorship.
*emmanuelle.helfer@univ-amu.fr, catherine.badens@univ-amu.fr

1. J Lammerding, et al., Lamins a and c but not lamin b1 regulate nuclear mechanics. *J. Biol. Chem.* **281**, 25768–25780 (2006).
2. F Guilak, JR Tedrow, R Burgkart, Viscoelastic properties of the cell nucleus. *Biochem. biophysical research communications* **269**, 781–786 (2000).
3. JL Broers, et al., Decreased mechanical stiffness in lmna-/- cells is caused by defective nucleo-cytoskeletal integrity: implications for the development of laminopathies. *Hum. molecular genetics* **13**, 2567–2580 (2004).
4. J Lammerding, et al., Lamin a/c deficiency causes defective nuclear mechanics and mechanotransduction. *The J. clinical investigation* **113**, 370–378 (2004).
5. P Isermann, J Lammerding, Nuclear mechanics and mechanotransduction in health and disease. *Curr. Biol.* **23**, R1113–R1121 (2013).
6. J Hah, DH Kim, Deciphering nuclear mechanobiology in laminopathy. *Cells* **8**, 231 (2019).
7. Y Kim, X Zheng, Y Zheng, Role of lamins in 3d genome organization and global gene expression. *Nucleus* **10**, 33–41 (2019).
8. N Bonello-Palot, et al., Prelamin a accumulation in endothelial cells induces premature senescence and functional impairment. *Atherosclerosis* **237**, 45–52 (2014).
9. M Caron, et al., Human lipodystrophies linked to mutations in a-type lamins and to hiv protease inhibitor therapy are both associated with prelamin a accumulation, oxidative stress and premature cellular senescence. *Cell Death & Differ.* **14**, 1759–1767 (2007).
10. V Cenni, et al., Lamin a involvement in ageing processes. *Ageing Res. Rev.* **10**, 101073 (2020).
11. C López-Otín, MA Blasco, L Partridge, M Serrano, G Kroemer, The hallmarks of aging. *Cell* **153**, 1194–1217 (2013).
12. AA Varlet, E Helfer, C Badens, Molecular and mechanobiological pathways related to the physiopathology of fpld2. *Cells* **9**, 1947 (2020).
13. T Dechat, et al., Nuclear lamins: major factors in the structural organization and function of the nucleus and chromatin. *Genes & development* **22**, 832–853 (2008).
14. Sm Kang, MH Yoon, BJ Park, Laminopathies; mutations on single gene and various human genetic diseases. *BMB reports* **51**, 327 (2018).
15. J Zammouri, et al., Molecular and cellular bases of lipodystrophy syndromes. *Front. endocrinology* **12** (2021).
16. KN Dahl, et al., Distinct structural and mechanical properties of the nuclear lamina in hutchinson–gilford progeria syndrome. *Proc. Natl. Acad. Sci.* **103**, 10271–10276 (2006).
17. EA Booth, ST Spagnol, TA Alcoser, KN Dahl, Nuclear stiffening and chromatin softening with progerin expression leads to an attenuated nuclear response to force. *Soft Matter* **11**, 6412–6418 (2015).
18. PM Davidson, et al., High-throughput microfluidic micropipette aspiration device to probe time-scale dependent nuclear mechanics in intact cells. *Lab on a Chip* **19**, 3652–3663 (2019).
19. O Wintner, et al., A unified linear viscoelastic model of the cell nucleus defines the mechanical contributions of lamins and chromatin. *Adv. Sci.* **7**, 1901222 (2020).
20. M Herbig, et al., Real-time deformability cytometry: label-free functional characterization of cells in *Flow cytometry protocols.* (Springer), pp. 347–369 (2018).
21. PM Davidson, J Sliz, P Isermann, C Denais, J Lammerding, Design of a microfluidic device to quantify dynamic intra-nuclear deformation during cell migration through confining environments. *Integr. Biol.* **7**, 1534–1546 (2015).
22. ML Heuzé, O Collin, E Terriac, AM Lennon-Duménil, M Piel, Cell migration in confinement: a micro-channel-based assay in *Cell Migration.* (Springer), pp. 415–434 (2011).
23. P Preira, MP Valignat, J Bico, O Théodoly, Single cell rheometry with a microfluidic constriction: quantitative control of friction and fluid leaks between cell and channel walls. *Biomicrofluidics* **7**, 024111 (2013).
24. J Dupire, PH Puech, E Helfer, A Viallat, Mechanical adaptation of monocytes in model lung capillary networks. *Proc. Natl. Acad. Sci. United States Am.* **0** (2020).
25. C Vatier, et al., One-year metreleptin improves insulin secretion in patients with diabetes linked to genetic lipodystrophic syndromes. *Diabetes, Obes. Metab.* **18**, 693–697 (2016).
26. RD Goldman, et al., Accumulation of mutant lamin a causes progressive changes in nuclear architecture in hutchinson–gilford progeria syndrome. *Proc. Natl. Acad. Sci.* **101**, 8963–8968 (2004).
27. RA Veitia, Dna content, cell size, and cell senescence. *Trends biochemical sciences* **44**, 645–647 (2019).
28. AD Stephens, et al., Chromatin histone modifications and rigidity affect nuclear morphology independent of lamins. *Mol. biology cell* **29**, 220–233 (2018).
29. VJ Tocco, et al., The nucleus is irreversibly shaped by motion of cell boundaries in cancer and non-cancer cells. *J. cellular physiology* **233**, 1446–1454 (2018).
30. A Dutour, et al., High prevalence of laminopathies among patients with metabolic syndrome. *Hum. molecular genetics* **20**, 3779–3786 (2011).
31. G Salbreux, G Charras, E Paluch, Actin cortex mechanics and cellular morphogenesis. *Trends Cell Biol.* **22**, 536–545 (2012).
32. JY Tinevez, et al., Role of cortical tension in bleb growth. *Proc. Natl. Acad. Sci.* **106**, 18581–18586 (2009).
33. E Fischer-Friedrich, AA Hyman, F Jülicher, DJ Müller, J Helenius, Quantification of surface tension and internal pressure generated by single mitotic cells. *Sci. reports* **4**, 1–8 (2014).
34. K Guevorkian, MJ Colbert, M Durth, S Dufour, F Brochard-Wyart, Aspiration of biological viscoelastic drops. *Phys. review letters* **104**, 218101 (2010).
35. GT Charras, M Coughlin, TJ Mitchison, L Mahadevan, Life and times of a cellular bleb. *Biophys. journal* **94**, 1836–1853 (2008).
36. K Sliogeryte, SD Thorpe, DA Lee, L Botto, MM Knight, Stem cell differentiation increases membrane-actin adhesion regulating cell blebability, migration and mechanics. *Sci. reports* **4**, 1–9 (2014).
37. C Denais, J Lammerding, Nuclear mechanics in cancer. *Cancer biology nuclear envelope*, 435–470 (2014).
38. H Haga, et al., Elasticity mapping of living fibroblasts by afm and immunofluorescence observation of the cytoskeleton. *Ultramicroscopy* **82**, 253–258 (2000).
39. C Rotsch, M Radmacher, Drug-induced changes of cytoskeletal structure and mechanics in fibroblasts: an atomic force microscopy study. *Biophys. journal* **78**, 520–535 (2000).
40. K Sliogeryte, N Gavara, Vimentin plays a crucial role in fibroblast ageing by regulating biophysical properties and cell migration. *Cells* **8**, 1164 (2019).
41. K Pogoda, et al., Depth-sensing analysis of cytoskeleton organization based on afm data. *Eur. Biophys. J.* **41**, 79–87 (2012).
42. R Mahaffy, S Park, E Gerde, J Käs, CK Shih, Quantitative analysis of the viscoelastic properties of thin regions of fibroblasts using atomic force microscopy. *Biophys. journal* **86**, 1777–1793 (2004).
43. I Dulińska-Molak, et al., Age-related changes in the mechanical properties of human fibroblasts and its prospective reversal after anti-wrinkle tripeptide treatment. *Int. journal peptide research therapeutics* **20**, 77–85 (2014).
44. PG de Gennes, F Brochard-Wyart, D Quéré, *Capillarity and Wetting Phenomena.* (2004).
45. D Borin, et al., Altered microtubule structure, hemichannel localization and beating activity in cardiomyocytes expressing pathologic nuclear lamin a/c. *Heliyon* **6**, e03175 (2020).
46. AT Molines, et al., Physical properties of the cytoplasm modulate the rates of microtubule polymerization and depolymerization. *Dev. Cell* **57**, 466–479 (2022).
47. BA Danowski, Fibroblast contractility and actin organization are stimulated by microtubule inhibitors. *J. Cell Sci.* **93**, 255–266 (1989).
48. A Rape, Wh Guo, YI Wang, Microtubule depolymerization induces traction force increase through two distinct pathways. *J. cell science* **124**, 4233–4240 (2011).
49. KL Hui, A Upadhyaya, Dynamic microtubules regulate cellular contractility during t-cell activation. *Proc. Natl. Acad. Sci.* **114**, E4175–E4183 (2017).
50. M Crisp, et al., Coupling of the nucleus and cytoplasm: role of the linc complex. *The J. cell biology* **172**, 41–53 (2006).
51. D Brayson, CM Shanahan, Current insights into lmna cardiomyopathies: Existing models and missing lincs. *Nucleus* **8**, 17–33 (2017).
52. M Mendez, D Restle, P Janmey, Vimentin enhances cell elastic behavior and protects against compressive stress. *Biophys. journal* **107**, 314–323 (2014).
53. GR Kidiyoor, et al., Atr is essential for preservation of cell mechanics and nuclear integrity during interstitial migration. *Nat. communications* **11**, 1–16 (2020).
54. C Desgrouas, et al., Unraveling lmna mutations in metabolic syndrome: Cellular phenotype and clinical pitfalls. *Cells* **9**, 310 (2020).
55. MATLAB, *version 9.40.0 (R208a).* (The MathWorks Inc., Natick, Massachusetts), (2018).

Supplementary information for: Enhanced cell viscosity as a marker of premature senescence induced by lamin A/C alterations

Cécile Jebane, Alice-Anaïs Varlet, Marc Karnat, Lucero M. Hernandez-Cedillo, Amélie Lecchi, Frédéric Bedu, Camille Desgrouas, Corinne Vigouroux, Marie-Christine Vantyghem, Annie Viallat, Jean-François Rupprecht, Emmanuèle Helfer and Catherine Badens

Corresponding to Emmanuèle Helfer and Catherine Badens:
emmanuelle.helfer@univ-amu.fr, catherine.badens@univ-amu.fr

This PDF file includes:
Supplementary text
Tables S1 to S2
References for SI reference citations
Figs. S1 to S13

A. Methods.

Cells, nuclei, treatments and senescence assays.

Cells. Fibroblasts are issued from two patients with FPLD2 due to the R482W heterozygous pathogenic variant of the *LMNA* gene (patients 8 and 12 in Ref. (1), referred to as patients K and M, respectively), and from a diabetic patient with no lamin A/C alteration (patient 17 in Ref. (2), referred to as patient T2D). Control and Progeria (HGPS) fibroblasts were purchased from Coriell Institute (AG07095, AG06917). Cell lines are summarized in Table 2.

Nucleus extraction. Nuclei were isolated following an adapted protocol from Ref. (3). Adherent cells were incubated in H_2O MQ + IGEPAL 0.05% + Citric Acid 1% for 5 min at 37°C. The flask was vigorously tapped to expel the nuclei. The flask content was harvested, and the nuclei were washed with 10 mL PBS, vortexed $\sim$ 10 s and centrifuged at 800 g for 5 min. The supernatant was removed and the nuclei in the pellet were resuspended in PBS + BSA 1%.

Cell treatments. Atazanavir (AZN) (from hospital, stock solution at 50 mM in DMSO) was added at varying concentration from 25 to 75 μM to the cell medium of control cells during 48 h before analyzing senescence-associated phenotypes. Fibroblasts were also treated with 200 nM latrunculin A (stock solution at 1 mM in DMSO; L5163, Sigma-Aldrich) or 10 μM nocodazole (stock solution at 50 mM in DMSO; 487928, Sigma-Aldrich) for 10 and 45 min, respectively, or both (35 min with nocodazole alone, then 10 more min with latrunculin A and nocodazole), before processing cells for experiments. For latrunculin A treatment, cells were incubated 35 min with DMSO prior to drug addition to keep 45 min total incubation with the carrier.

Senescence test through 5-bromo-2'-deoxyuridine (BrdU) incorporation. Cells were seeded on 96-well plate at a density of 10^4 cells/well and BrdU was added to the cell culture medium 24 h before performing an ELISA assay following the manufacturer instructions (Cell proliferation ELISA, BrdU (colorimetric) Kit, Roche Applied Science).

Senescence test through SA-β-galactosidase activity. Cells were seeded on glass coverslips (Lab-tek, SPL Life Sciences) coated with 100 μg/mL fibronectin (Sigma-Aldrich) and β-galactosidase activity was measured following the manufacturer instructions (Senescence β-Galactosidase Staining Kit, Cell Signaling Technology).

Fluorescence microscopy, cellular and nuclear volume quantification.

Immunofluorescence and microscopy. Immunofluorescence was performed on adhered cells after fixation with 4% PFA at room temperature (RT) for 10 min and permeabilization with 0.5% Triton® X-100 (Sigma-Aldrich) at RT for 10 min. After washing twice with PBS, saturation was performed with 1% BSA (37525, Thermofisher) for 30 min at RT. Cells were incubated with 150 ng/mL Hoechst 33342 (H3570, Thermofisher) for 15 min at RT prior to saturation with primary mouse anti-lamin A/C (1:1000, sc-376248, Santa Cruz) or anti-α-tubulin (1:1000, T5168, Sigma-Aldrich) antibodies for 1.5 h at 37 °C. After washing twice with PBS 0.1% tween, samples were incubated with an appropriate secondary antibody coupled with Alexa Fluor 488 (Invitrogen) for 1 h at 37 °C. When required actin staining was performed at the same time using Texas Red™-X Phalloidin (1:100, T7471, Thermofisher). Samples were then washed twice with PBS and post-fixed for 10 min with 4% PFA, before mounting on slides with ProLong™ Diamond Antifade Mountant (Thermofisher). Nuclear phenotypes were monitored using an ApoTome system (Zeiss), equipped with a 100× objective and a CCD camera (Axiocam MRm, Zeiss). Nuclear abnormality criteria were aberrant nuclear lamin A/C staining pattern, enlarged nucleus, and aberrant nucleus shape. At least 1000 cells were examined for each condition and the percentage of abnormal nuclei was calculated.

Cellular and nuclear volumes. Cellular and nuclear volumes were determined from confocal microscopy images. Adhered cells were incubated for 1 h with CellBrite™ Green (Biotum) and 5 mg/mL Hoechst, then detached using 0.05% Trypsin-EDTA (25300-054, Gibco). Cells were resuspended in complete cell medium supplemented with 1 mM HEPES and deposited on glass coverslips coated with 0.1 mg/mL PLL-PEG (PLL(20)-g[3.5]PEG(5), SuSoS AG) in 10 mM HEPES pH 7.4 to prevent cell adhesion. Cells in suspension were subsequently observed on a confocal microscope (LSM 800 airyscan Axio Observer Z1 7, Zeiss) equipped with a 63× water objective (63x/1.20 W Korr UV VIS IR C-Apochromat, Zeiss). Z-stacks were acquired with a 0.5-μm z-step in fluorescence channels corresponding to Cell Brite and Hoechst labeling. FIJI software (ImageJ) was used for volume quantification using a home-made macro: 1) the z-stack was thresholded; 2) for each stack slice i the object (cell or nucleus) contour was determined and its area Area_i was measured (in μm^2); 3) the volume was calculated by summing the slice volumes: $V = \Sigma_i \text{Area}_i \times \delta h$, with $\delta h = 0.5$ μm (z-step between slices). It must be noted that the nuclei are wrinkled when cells are in suspension (Fig. 11), as previously reported (4, 5). Here, the wrinkles were neglected in the estimation of the nuclear volumes.

Microfluidic device fabrication. The microfluidic device is in polydimethylsiloxane (PDMS) and consists of a chamber made of a bottom PDMS-coated glass coverslip (defined as "bottom coverslip") assembled with a few mm-thick PDMS piece with channels dug in it (defined as "microchannel").

Microchannel. The microchannel was fabricated from a master mold created on a silicium wafer using standard photolithography performed at PLANETE microfabrication facility of the laboratory (Fig. 12). Three masks were used to create the mold: (1) alignment crosses, (2) main channel with micrometer-sized constrictions in the central part, and (3) main channel without constrictions. A negative tone resist (AR-N 4340, AllResist) was spin-coated at 4000 rpm for 1 min on the silicium wafer before a first soft baking step at 85°C for 2 min, followed by exposure to UV for 14 s using mask (1) positioned with an aligner (MJB4 aligner, Carl Suss). A post-exposure baking step was performed (95°C, 2 min) before the resist layer was developed with a developer (AR300-475, Allresist). Next, a thin 160-nm aluminum (Al) layer was deposited by sputtering. A lift-off step was performed overnight with a solvent (NMP, MicroChemicals) to remove the resist which has not been exposed to UV and the Al deposited on it, leaving only the alignment crosses. To enhance adhesion between the resist and the silicium wafer, the wafer was plasma-treated for 10 min before an adhesion promotion layer (Omnicoat™, MicroChemicals) was spin-coated (3000 rpm,

40 s) then baked (200°C, 1 min). Permanent Epoxy Negative Photoresist (SU8-2005, MicroChemicals) was spin-coated on the wafer (1500 rpm, 60 s) to obtain a 6-μm layer before soft baking (9°C, 2 min). The resist was then aligned with mask (2) using Al crosses and exposed to UV for 10 s. The resist-coated wafer was then post baked (95°C, 3 min), developed in SU8-Developer (DevSU8/4, MicroChemicals) to remove unpolymerized resist, washed abundantly with isopropanol, air-blown and hard baked (cured) at 150°C for 5-10 min to prevent the resist from cracking. The process was repeated with mask (3) to create a second 4-μm layer, with diluted SU8-2005 (90% v/v in cyclopentanone). After fabrication, the mold was treated once with silane Trichloro(1H,1H,2H,2H-perfluorooctyl)silane (448931, Sigma-Aldrich) to prevent PDMS from sticking and subsequently damaging the constrictions. A mold is typically used at least ten times, until it starts showing signs of deterioration. A 10:1 mixture of PDMS and cross-linking agent (Sylgard 184, Dow Corning) was poured on the master mold. After degassing in a vacuum chamber for 30 min and curing at 80°C for 2 h up to overnight, the PDMS microchannel was peeled off from the mold.
Bottom coverslip. Glass coverslips were cleaned by sonication in acetone then in isopropanol, for 30 min each, washed in ethanol for 5 min, and rinsed abundantly with MilliQ water. Cleaned coverslips were stored in MilliQ water until used. A few drops of PDMS was poured onto a dried coverslip and spin-coated at 4000 rpm for 45 s before being cured at 80°C overnight.
Chip assembly. The three inlets and the outlet of the PDMS microchannel were drilled with a 0.75-mm punch (Biopsy Punch 504529, World Precision Instruments) prior to assembling the microfluidic chip by bonding the microchannel to the bottom coverslip via plasma treatment, followed by a curing step at 80 °C overnight.

Microfluidic experiment. The experiments were performed on a microscope (IX71, Olympus) equipped with a 20× objective and high-speed cameras (Fastcam Mini UX, Photron and VEO310, Phantom) at 37°C. Prior to experiments, cells were cultured for 72 h (including 48 h of AZN treatment), to ensure ≈90% cell confluence. The microfluidic chip inlets and oulet were connected via Teflon tubing (0.012" inner diameter (ID) and 0.030" outer diameter (OD), BB311-30, Scientific Commodities Inc.) to a pressure controller (MFCS™-EZ 1000 mbar, FLUIGENT) that allows controlling the pressure drop between inlets and outlet and thus the circulation of cells/nuclei in suspension. Microchannels were passivated with 10% Pluronic®F-127 (P2443, Sigma) in PBS for 1 h at RT. Inlets (1) and (3) were used to inject buffer solutions while cells/nuclei were injected with inlet (2) (see Fig. 2A for a schematic view of the chip).
Cell experiment. Cells suspended in complete medium supplemented with 10 mM HEPES, 1% BSA (± cytoskeleton drugs) were injected in microchannels under a pressure drop of $\Delta P = 165$ mbar ($P_{inlets} = 170$ mbar, $P_{oulet} = 5$ mbar). Cells were observed in brightfield and movies were acquired at frame rates varying from 125 to 1000 fps.
Isolated nucleus experiment. Isolated nuclei suspended in PBS with 1% BSA were injected in microchannels under a pressure drop of $\Delta P = 200$ mbar ($P_{inlets} = 205$ mbar, $P_{oulet} = 5$ mbar). Nuclei were observed in epifluorescence and movies were acquired between 500 and 1000 fps.

Image processing and analysis.
Cell analysis. Movies were pre-processed using FIJI software. To enhance cell contrast and remove constrictions (static in the movie), a median image from a few frames was computed and a new movie was produced by subtracting the median image. Using Non-Local Mean Denoising Plugin (6, 7), the background noise was removed while keeping the cell intact, which was then manually thresholded. Using Matlab software (r2018b version, MathWorks (8)), a bounding box was fitted around the thresholded cell at each time point to measure the cell dimensions (length L along the flow axis and width w perpendicularly to it) over time.
Isolated nucleus analysis. Movies were pre-processed using FIJI software, with automated tracking of individual nuclei using Trackmate (9). Each track contained the X-Y positions of a nucleus centroid at each timepoint. Using the X-Y positions of the centroids, we defined an initial mask of 12×12 pixels that evolved to perfectly fit the nucleus contour using the Active Contour method in Matlab (10, 11). Once the final contour was retrieved, the image was segmented and the bounding box analysis was performed such as for cells.
Cellular and nuclear volumes. Additionally, volumes of cells and isolated nuclei were computed from microfluidic images before contact with constrictions, assuming they have a "pancake" shape. The volume is computed as the projected area multiplied by the microfluidic channel height: $V = \text{area} \times h_1$.

Tongue length analysis.
Entry time and slope analysis. With a home-made Matlab routine, the time evolution of the tongue length $\ell(t)$ was plotted and four parameters were manually determined: the entry time T_e (in s), defined as the time the cell takes to fully enter a constriction, and three slopes S_1 to S_3 (in s^{-1}) corresponding to three distinct regimes displayed during the cell entry and considered as linear in a first approximation. To calculate the slopes, the first and last points of each regime were selected, and a tangent was automatically fitted that provided the slope value.
Rheological fit. Matlab fit function (8) was used on the curves ℓ(t), with expression `a (1-exp(-bt)) + ct`, where a, b, and c are fit parameters; the combination of these parameters provides the physical quantities defined in Eq. (8). We performed a series of 6 fits of the experimental curves with a set of time intervals $I_m = [0; m \times T_e/10]$ with $m = 4, \ldots, 10$, where T_e is the cell entry time. For each fit, we evaluated the corresponding physical parameters and R^2 chi-square values, and defined for each cell the following lists: $(\eta_2^{(m)})_{m=4,\ldots,10}$, $(\eta_1^{(m)})_{m=4,\ldots,10}$, $(E^{(m)})_{m=4,\ldots,10}$ and $(R^{2(m)})_{m=4,\ldots,10}$. We only retained fitted parameters whose corresponding fits had the maximal R^2 value that is larger than a critical threshold set at 0.85, i.e. those such that $R_I^2 = \max(R_m^2)_{m=4,\ldots,10} > 0.85$. We discarded too large values of $\eta_2 > 10^5$ Pa.s, $\eta_1 > 500$ Pa.s and $E > 70$ kPa –

threshold values one to two orders of magnitude larger than typical median values. We also discarded too low values of $\eta_1 < 5$ Pa.s and $E < 0.7$ kPa.

Statistical analysis. When indicated, N, n, and n' are the number of experiments, of analyzed cells, and of fitted curves, respectively. Statistical calculations were performed using Prism 6.0 statistical software (GraphPad). Significant differences (p-values) are indicated with stars (or #,¤): *, $p < 0.05$; **, $p < 0.01$; ***, $p < 0.001$; ****, $p < 0.0001$. – For experiments examining the proportions of cells with nuclear abnormalities or SA-β-galactosidase positive staining, data were averaged over at least 3 independent experiments (mean ± SD, standard deviation) and mean values were compared using the Fisher's exact test and the Bonferroni post-hoc analysis to correct for multiple comparisons. – For BrdU incorporation, data were averaged over at least 3 independent experiments (mean ± SD) for each condition, and mean values were compared using the Kruskal-Wallis test followed by the Dunn's multiple comparison post-hoc analysis when appropriate. – For nuclear and cellular volumes, the median values and 95% Confidence Intervals (CIs) were calculated from measurements on individual cells pooled from at least 2 independent experiments, and median values were compared using the Kruskal-Wallis test followed by the Dunn's multiple comparison analysis. – Entry time, tongue length slopes, and rheological parameters derived from the fits of the tongue length curves all displayed non-Gaussian distributions. The median values were calculated with 95% CIs from individual cells pooled from at least 3 independent experiments, and data were compared using the Kruskal-Wallis test followed by the Dunn's multiple comparison analysis.

B. Rheological models. We derived the elastic modulus and the viscosities of cells using a viscoelastic model as laid out in previous works using micropipettes (12, 13), with adaptation for a squared cross-section constriction.

Constant pressure drop approximation. In Ref. (12), aspiration is performed using a cylindrical pipette of circular cross-section πR_p^2. Considering volume conservation (experimentally, the cell volume decreases at most by 20%), the aspiration force under a pressure drop ΔP between the exterior and the interior of the pipette reads

$$f = \pi R_p^2(\Delta P - \Delta P_c) \approx \pi R_p^2 \Delta P \quad [1]$$

Here we argue that the effective stress is essentially the applied pressure drop and that the Laplace pressure ΔP_c, which is the critical pressure required to push cells through constrictions, can be neglected. Indeed,

$$\Delta P_c \approx 2\gamma \left(\frac{1}{R_{\text{in}}} - \frac{1}{R_{\text{out}}} \right), \quad [2]$$

where the cell radii $R_{\text{in}} = R_p$ and R_{out} correspond to the portion of the cell either inside (font of the cell) or outside (back of the cell) the constriction, respectively, and γ is the cortical surface tension. The cortical tension lies in the 5.10^{-4} N.m^{-1} (cortical tension in fibroblast cells (14, 15)), with upper values reported at 2.10^{-3} N.m^{-1} (dividing Hela cells (16)), corresponding to ΔP_c in the 0.5 to 2 kPa range. In comparison, the applied pressure drop is $\Delta P = 165$ mbar $= 16.5$ kPa, which is significantly larger than ΔP_c. Considering a more realistic geometry with a Laplace pressure given as in Ref. (17) does not affect our conclusion. In addition, the validity of our approximation is verified a posteriori through the estimation of a capillary number based on the measured the cell viscosity (see main text, Discussion). We point out that Ref. (18), which focuses on the measure of surface tension, considered a significantly lower applied pressure.

Jeffreys rheological model. An established literature (12, 13, 19) models the evolution of the deformation of various objects (from nuclei to cell aggregates) in micropipettes through a Jeffreys rheological model. Here we propose the Jeffreys model results in the following time evolution of the aspirated tongue length (13).

$$\ell(t) = \frac{f}{k}\left(1 - e^{-t/\tau}\right) + \frac{f}{\mu_2} t \quad [3]$$

where f is the applied force, defined in Eq. (1), k is a spring constant, τ is a relaxation time and μ_2 is the long-time viscosity. The first term in Eq. (3) describes the short time behavior, during which the pressure force is balanced by the cell elastic forces. The cell yields after a characteristic time τ, which we can express in terms of a short-time viscosity μ_1 as $\tau = k/\mu_1$. The second term in Eq. (3) describes the long time behavior (before complete cell entrance is achieved) during which the pressure force is balanced by the viscous force due to a plug flow at the entrance of the capillary, leading to a linear increase of the regime strain with time. The stress/strain relation of Eq. (3) is commonly represented diagrammatically in terms of a Kelvin-Voigt element, i.e., a spring (k) and a dashpot ($\mu_1 = k/\tau$) in parallel, in series with a dashpot (μ_2).

Relation to rheology. Here we propose to map the spring k, viscoelastic time τ and viscosity μ_2 parameters defined in Eq. (3) to a simplified model for the cell rheological properties. Following the literature (12, 13), we discuss the expected behavior of the cell considered as a homogeneous viscoelastic material under aspiration through a cylindrical constriction of radius R_p.

At short time scales, the aspiration force is balanced by the elastic deformation and is given by the following equation:

$$\frac{f}{A} = CE\frac{\delta}{R_p}, \quad [4]$$

where $A = \pi R_p^2$ is the cross-sectional area of the constriction, C is a geometrical factor approximately equivalent to 1 (12, 13), E is the elastic modulus and δ is the elastic deformation at short times. We thus obtain $f = \pi R_p E \delta$. The spring constant k is the coefficient between the applied force f and the extension δ, $f = k \times \delta$, leading to the relation

$$k = \pi R_p E. \quad [5]$$

At long time scales, the aspiration force is balanced by two dissipation forces. The first one arises from the viscous flow of the cell through the entrance of the constriction, such as the flow of a viscous fluid through a circular pore described by Sampson (20). The second source of dissipation arises from the resistance of the tongue slipping along the constriction wall. Combining both terms leads to (12, 21)

$$f = 3\pi^2 \eta_2 R_p \dot{\ell} + 2\pi \xi R_p \ell \dot{\ell}, \quad [6]$$

where η_2 is the cell effective viscosity and ξ is the cell-wall friction coefficient. As in Refs. (12) and (13), we can ignore the friction on the surface of the constriction: indeed, once the cell has fully entered into the constriction, its velocity (in the $50\,\mu\text{m.s}^{-1}$ range) is significantly larger than during the deformation phase. Identifying $\dot{\ell} = f/\mu_2$ from the second term in Eq. (3) leads to

$$\mu_2 = 3\pi^2 \eta_2 R_p. \quad [7]$$

Inserting Eqs. (5) and (7) into Eq. (3), we obtain the following relation of the cell tongue length as a function of the cell rheological properties:

$$\ell(t) = \frac{R_p \Delta P}{E}\left(1 - e^{-\frac{E}{3\pi\eta_1}t}\right) + \frac{R_p \Delta P}{3\pi\eta_2}t, \quad [8]$$

that we use within the main text.

A key interest of Eq. (8) is to provide a set of intensive mechanical properties that allows comparison between classes of cell types. For each cell type, we verified that the estimated mechanical parameters in Eq. (8) did not vary for cells of different sizes (see Fig. 13).

Effective radius of the constriction. For a cylindrical pipette as in Ref. (12), the pipette radius R_p is used in Eq. (1). In our case, the constrictions are rectangular instead of cylindrical and R_p is replaced by an effective radius R_{eff} that is the function of the height and width of the rectangular cross-section. Following Ref. (13) and the theoretical study in Ref. (22), we express the effective radius as

$$R_{\text{eff}}^4 = \frac{2}{\pi}\frac{w \times h_1^3}{(1 + h_1/w)^2 \times g^*(h_1/w)}, \quad [9]$$

where h_1 and w are the dimensions of the constriction cross-section and g^* is a dimensionless function of the form

$$g^*(x) = \left[\left(1 + \frac{1}{x}\right)^2 \left(1 - \frac{192}{\pi^5 x}\sum_{i=1,3,5}^{\infty}\frac{\tanh\left(\frac{\pi}{2}ix\right)}{i^5}\right)\right]^{-1}. \quad [10]$$

With $w = h_1 = 6\,\mu\text{m}$, applying Eq. (9) yields $R_{\text{eff}} = 4.32\,\mu\text{m}$.

We point out that Eq. (9) is not strictly exact in our case, since our geometry is off-centered in height, which is not exactly the case considered in Ref. (22). Nonetheless, we expect R_{eff} to be a satisfactory approximation. In addition, in our study the constriction geometry is identical for all cell types and drug treatment; any approximation on the value of R_{eff} will not affect conclusions based on the comparisons of mechanical parameters between experiments.

A simple power law between cell initial length L_0 and entry time T_e allows for crossed comparisons of viscous moduli. Here we propose to extract a simple relation between the entry time T_e and the cell radius before entry that holds for sufficiently large cells. In this case $T_e \gg \tau$ on average and, by neglecting the time spent in both phases I and III (see Fig. 2D in main), the aspirated tongue length at time T_e derives from Eq. (8) as

$$\ell(T_e) \approx \frac{R_{\text{eff}} \Delta P}{E} + \frac{R_{\text{eff}} \Delta P}{3\pi\eta_2} T_e. \quad [11]$$

Assuming the cell has a disk shape of diameter L_0 before entering the constriction, the initial volume V_i can be expressed as $V_i = \pi(L_0/2)^2 h_1$. Once fully entered in the constriction, the cell shape is approximately a parallelepiped of final length $\ell(T_e)$ and final volume $V_f \approx \ell(T_e) w h_1$. Considering the cell volume to be conserved, the final aspirated tongue length $\ell(T_e)$ can be expressed in terms of L_0 as:

$$\ell(T_e) \approx \pi \frac{L_0^2}{4w}. \quad [12]$$

Substituting the latter expression into Eq. (11), we obtain, for large cells $L_0/w \gg 1$, the following approximate scaling of the entry time T_e with the initial cell diameter (or initial length) L_0:

$$T_e \approx \frac{3\pi^2 \eta_2}{4w R_{\text{eff}} \Delta P} L_0^2. \quad [13]$$

Eq. (13) provides a rationale for fitting the relation between the experimental entry time T_e and the cell diameter L_0 through the following log-log scaling:

$$\log_{10}(T_e) = \log_{10}(\nu) + 2\log_{10}(L_0), \quad [14]$$

where we expect the quantity ν to be proportional to the long-time cell viscosity η_2, based on Eq. (13) (see Fig. 9B). We measure the value of ν for all cells whose experiment time is long enough ($T_e > 10\tau \approx 0.3$ s).

Alternative model: power-law rheology. Following Refs. (13, 23), we also evaluate the efficiency of a power-law fit of the tongue length data. We employ a similar fitting procedure as the one previously used for viscosity extraction, with a master curve:

$$\ell(t) = \ell_0 + \frac{t^\alpha}{A_\alpha}, \qquad [15]$$

where ℓ_0 corresponds to the very short-time elastic response and A_α is a quantity that corresponds to a non-Newtonian viscous coefficient (in the limit $\alpha = 1$, A_α corresponds to a Newtonian viscosity). Inspired by the range of values measured in Ref. (13), we set the value of the exponent to $\alpha = 0.5$. We then observe that the relations between the $1/A_\alpha$ prefactors in all cell types also correspond to the previously measured relations on η_2 (see Fig. 10). No outliers were filtered after this operation.

UNT				
	DMSO	N	L	NL
T_e (s)	0.48 [0.34-0.60]	0.26 [0.21-0.33]	0.22 [0.18-0.31]	0.15 [0.11-0.18]
η_2 (Pa.s)	251 [217-318]	287 [242-335]	146 [112-191]	91 [78-116]
τ (ms)	43 [38-50]	45 [38-53]	17 [15-21]	20 [16-24]
E (kPa)	5.7 [5.1-6.1]	6.2 [5.6-6.6]	4.5 [4.2-4.9]	4.5 [4.0-5.0]
η_1 (Pa.s)	26 [22-29]	29 [24-32]	9 [7-11]	10 [8-12]
AZN				
	DMSO	N	L	NL
T_e (s)	1.75 [1.33-2.12]	0.95 [0.75-1.20]	0.49 [0.42-0.66]	0.43 [0.36-0.55]
η_2 (Pa.s)	700 [582-844]	416 [333-506]	244 [190-302]	181 [138-227]
τ (ms)	55 [52-61]	68 [54-79]	23 [20-27]	25 [18-30]
E (kPa)	4.0 [3.9-4.3]	4.7 [4.4-5.0]	4.1 [3.8-4.3]	3.9 [3.6-4.3]
η_1 (Pa.s)	25 [23-28]	34 [28-39]	10 [8-11]	13 [6-16]
K				
	DMSO	N	L	NL
T_e (s)	1.26 [0.96-1.49]	0.56 [0.42-0.76]	0.54 [0.40-0.68]	0.41 [0.29-0.59]
η_2 (Pa.s)	631 [541-725]	293 [247-343]	219 [171-304]	168 [142-219]
τ (ms)	53 [46-57]	47 [42-53]	25 [21-30]	26 [20-30]
E (kPa)	4.1 [3.7-4.5]	4.2 3.8-4.6]	3.8 [3.6-4.4]	3.9 [3.4-4.3]
η_1 (Pa.s)	23 [19-27]	23 [19-25]	11 [8-13]	11 [9-14]

Table 1. Rheological parameters upon cytoskeleton disruption in UNT, AZN and K cells (medians [95% CI]). Colors indicate significant differences between N/L/NL *vs* DMSO conditions: ns * ** * ****. N = nocodazole, L = latrunculine A, NL = nocodazole + latrunculin A.**

Cell	Denotation	Description	Age	Sex	Biopsy source	Origin
AG07095	UNT	Apparently healthy individual	2	M	Foreskin	Purchased from Coriell Institute
AG06917	HGPS or Progeria	*LMNA* G608G mutation, HGPS	3	M	Arm	Purchased from Coriell Institute
Patient M*	FPLD2 M or M	*LMNA* R482W mutation, FPLD2	36	F	Skin	patient 12 (1)
Patient K*	FPLD2 K or K	*LMNA* R482W mutation, FPLD2	41	F	Skin	patient 8 (1)
Patient T2D*	T2D	No *LMNA* mutation, diabetic	49	M	Skin	patient 17 (2)

Table 2. Summary of fibroblast cell lines. * Patient 8 and 12 cells from Ref. (1), patient 17 cells from Ref. (2). Informed consent was obtained from all patients. Patients were unrelated.

Patients K and M, affected by FPLD2 associated with R482W mutation in the *LMNA* gene, presented similar symptoms such as peripheral lipoatrophy, fat accumulation in face and neck, muscular hypertrophy, fatty liver, hypertriglyceridemia, diabetes. Patient K had a more severe form of Dunnigan syndrome than patient M: lower amount of body fat, antecedent of acute pancreatitis at age 19, very severe insulin resistance, and diabetes was complicated by retinopathy and nephropathy. Patient T2D, who does not carry any *LMNA* mutation, presented neuromuscular complaint, fatty liver, severe hypertriglyceridemia, and diabetes.

1. C Vatier, et al., One-year metreleptin improves insulin secretion in patients with diabetes linked to genetic lipodystrophic syndromes. *Diabetes, Obes. Metab.* **18**, 693–697 (2016).
2. A Dutour, et al., High prevalence of laminopathies among patients with metabolic syndrome. *Hum. molecular genetics* **20**, 3779–3786 (2011).
3. GR Kidiyoor, et al., Atr is essential for preservation of cell mechanics and nuclear integrity during interstitial migration. *Nat. communications* **11**, 1–16 (2020).
4. DH Kim, et al., Volume regulation and shape bifurcation in the cell nucleus. *J. cell science* **128**, 3375–3385 (2015).
5. A Lomakin, et al., The nucleus acts as a ruler tailoring cell responses to spatial constraints. *Science* **370** (2020).
6. A Buades, B Coll, JM Morel, Non-local means denoising. *Image Process. On Line* **1**, 208–212 (2011).
7. J Darbon, A Cunha, TF Chan, S Osher, GJ Jensen, Fast nonlocal filtering applied to electron cryomicroscopy in *2008 5th IEEE International Symposium on biomedical imaging: from nano to macro*. (IEEE), pp. 1331–1334 (2008).
8. MATLAB, *version 9.40.0 (R2018a)*. (The MathWorks Inc., Natick, Massachusetts), (2018).
9. K Jaqaman, et al., Robust single-particle tracking in live-cell time-lapse sequences. *Nat. methods* **5**, 695–702 (2008).
10. S Lankton, Active contour segmentation (2016).
11. P Getreuer, Chan-vese segmentation. *Image Process. On Line* **2**, 214–224 (2012).
12. K Guevorkian, MJ Colbert, M Durth, S Dufour, F Brochard-Wyart, Aspiration of biological viscoelastic drops. *Phys. Rev. Lett.* **104**, 218101 (2010).
13. PM Davidson, et al., High-throughput microfluidic micropipette aspiration device to probe time-scale dependent nuclear mechanics in intact cells. *Lab on a Chip* **19**, 3652–3663 (2019).
14. G Salbreux, G Charras, E Paluch, Actin cortex mechanics and cellular morphogenesis. *Trends Cell Biol.* **22**, 536–545 (2012).
15. JY Tinevez, et al., Role of cortical tension in bleb growth. *Proc. Natl. Acad. Sci. United States Am.* **106**, 18581–18586 (2009).
16. E Fischer-Friedrich, AA Hyman, F Jülicher, DJ Müller, J Helenius, Quantification of surface tension and internal pressure generated by single mitotic cells. *Sci. Reports* **4**, 4–11 (2014).
17. H Bruus, *Theoretical Microfluids*. (2008).
18. J Dupire, PH Puech, E Helfer, A Viallat, Mechanical adaptation of monocytes in model lung capillary networks. *Proc. Natl. Acad. Sci. United States Am.* **117**, 14798–14804 (2020).
19. O Wintner, et al., A Unified Linear Viscoelastic Model of the Cell Nucleus Defines the Mechanical Contributions of Lamins and Chromatin. (2020).
20. RA Sampson, Xii. on stokes's current function. *Philos. Transactions Royal Soc. London.(A.)*, 449–518 (1891).
21. K Piroird, C Clanet, D Quéré, Capillary extraction. *Langmuir* **27**, 9396–9402 (2011).
22. Y Son, Determination of shear viscosity and shear rate from pressure drop and flow rate relationship in a rectangular channel. *Polymer* **48**, 632–637 (2007).
23. KN Dahl, et al., Distinct structural and mechanical properties of the nuclear lamina in hutchinson–gilford progeria syndrome. *Proc. Natl. Acad. Sci.* **103**, 10271–10276 (2006).

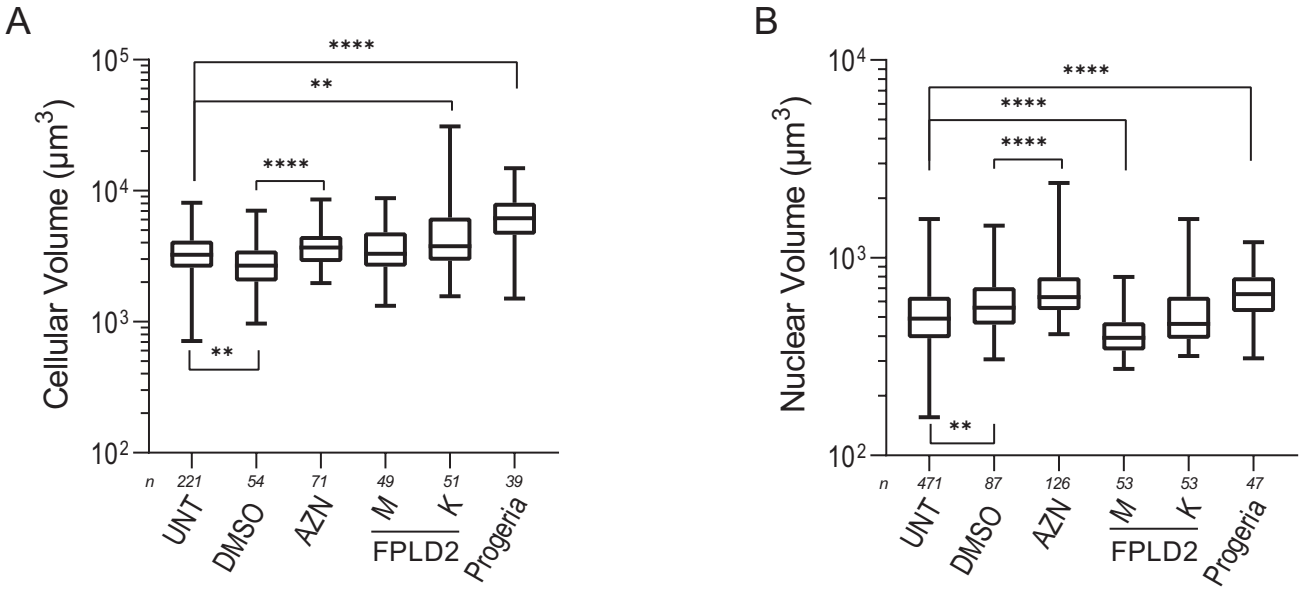

C

Cell	Cellular Volume (μm^3)		Nuclear Volume (μm^3)	
	Median	95% CI	Median	95% CI
UNT	3254	3068-3457	491	469-511
DMSO	2678	2294-3022	558	511-598
AZN	3677	3192-4205	633	591-686
FPLD2 M	3310	2986-3731	393	350-432
FPLD2 K	3775	3490-4495	462	413-578
Progeria	6171	4976-7635	654	568-737

Fig. 1. Cellular and nuclear volumes of control and senescent cells. UNT: untreated control cells; DMSO: control cells incubated with DMSO for 48 h; AZN: control cells treated with AZN (in DMSO) for 48 h; M,K: cells from two patients with FLPD2 carrying the lamin A/C R482W mutation; Progeria: cells from a patient with HGPS carrying the lamin A/C G608G mutation. Adhered cells were labelled for plasma membrane (with Cell Brite) and nuclei (with Hoechst) before detachment and resuspension in culture medium. Cellular and nuclear volumes were computed from confocal imaging. A-B) Boxplot representations of the cellular (A) and nuclear (B) volumes, with median values, 25% and 75% percentiles, and min/max values as whiskers. Number of experiments: N $\geq$ 2; number of analyzed cells: *n.* C) Table recapitulating median values of the volumes and 95% Confidence Intervals (CIs).

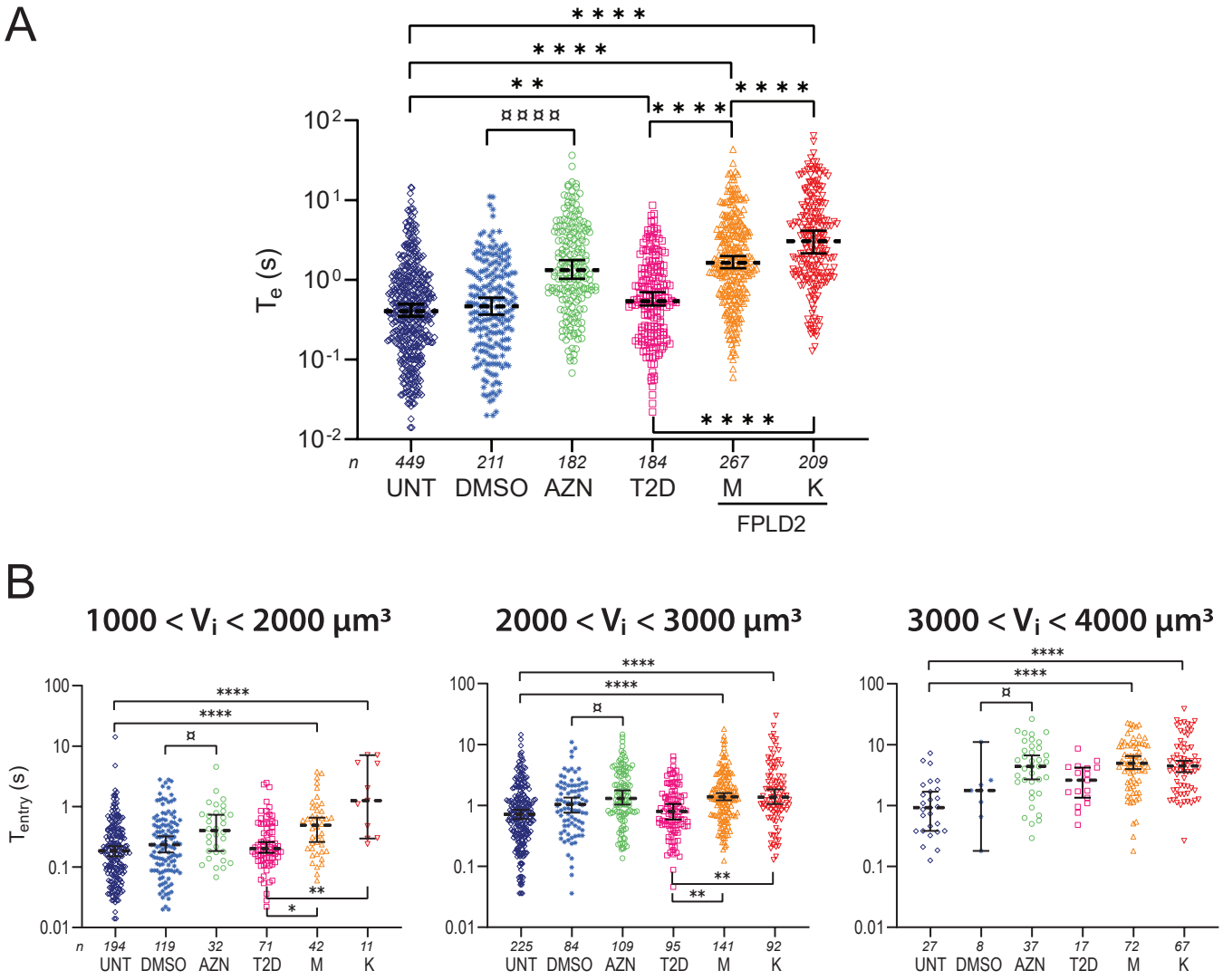

Fig. 2. Entry time in constrictions T_e is larger in senescent cells independently of cell size. Cell types as in Fig. 3: UNT: untreated control cells; DMSO: control cells incubated with DMSO for 48 h; AZN: control cells treated with AZN for 48 h; T2D: cells from the diabetic patient; M,K: cells from the patients with FPLD2. A) Dotplot representation of T_e, independently of cell size. The non-Gaussian distributions are plotted in log scale; median values and 95% CIs are indicated. The plots correspond to the bar plots in Fig. 3A and illustrate the number of analysed cells. B-E) Same plots as in (A), with cells sorted into three size populations. The cellular volumes were computed from the images of the cells before they enter the microfluidic constrictions. Both types of senescent cells, FPLD2 and AZN, display larger T_e compared to their respective controls, whatever the volume range. Significant differences: FPLD2 and L *vs* UNT cells, *; AZN *vs* DMSO cells, ¤. Number of experiments: N $\geq$ 3; number of analyzed cells: *n*.

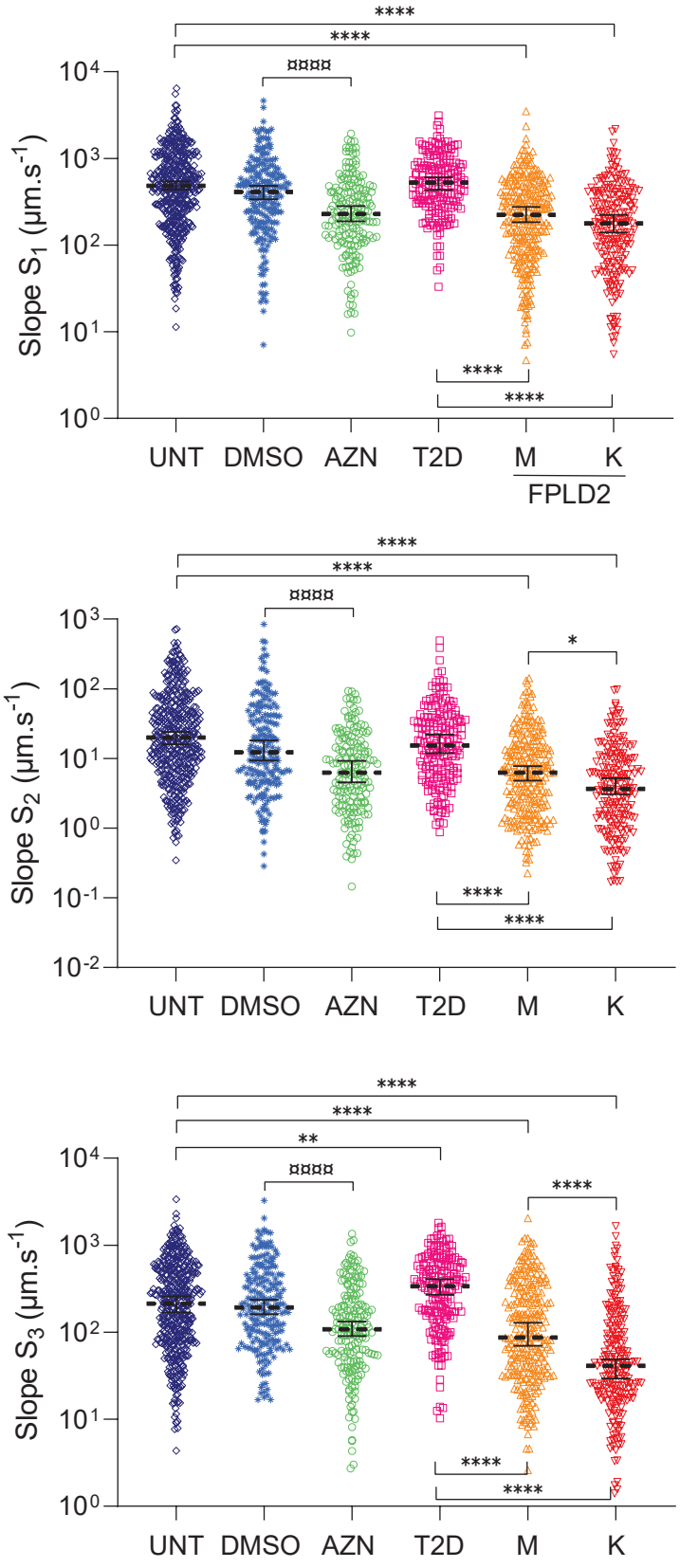

Fig. 3. The linear slopes $S_1 - S3$ of the three regimes in the temporal curve of the tongue length $\ell(t)$ are affected similarly to entry time T_e by the cell type. Cell types as in Figs. 3 and S2. Significant differences: FPLD2 and T2D *vs* UNT cells, *; AZN *vs* DMSO cells, ¤. Number of experiments: N $\geq$ 3; number of analyzed cells: n > 150.

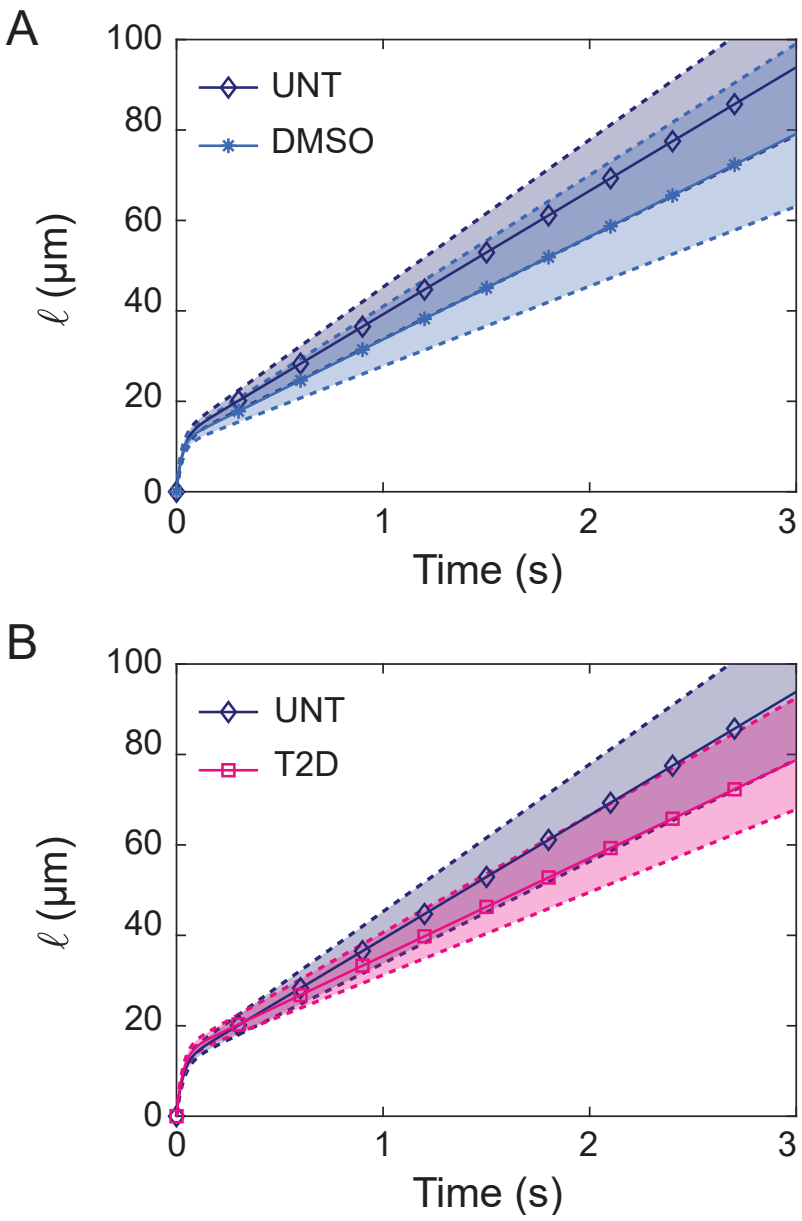

Fig. 4. Cells incubated with DMSO and cells from diabetic patient (T2D) behave like untreated control cells (UNT). Tongue length fits of (A) DMSO *vs* UNT cells, and (B) T2D *vs* UNT cells. Solid curves and symbols indicate the median fits, dashed upper and lower curves delineate the 95% CIs.

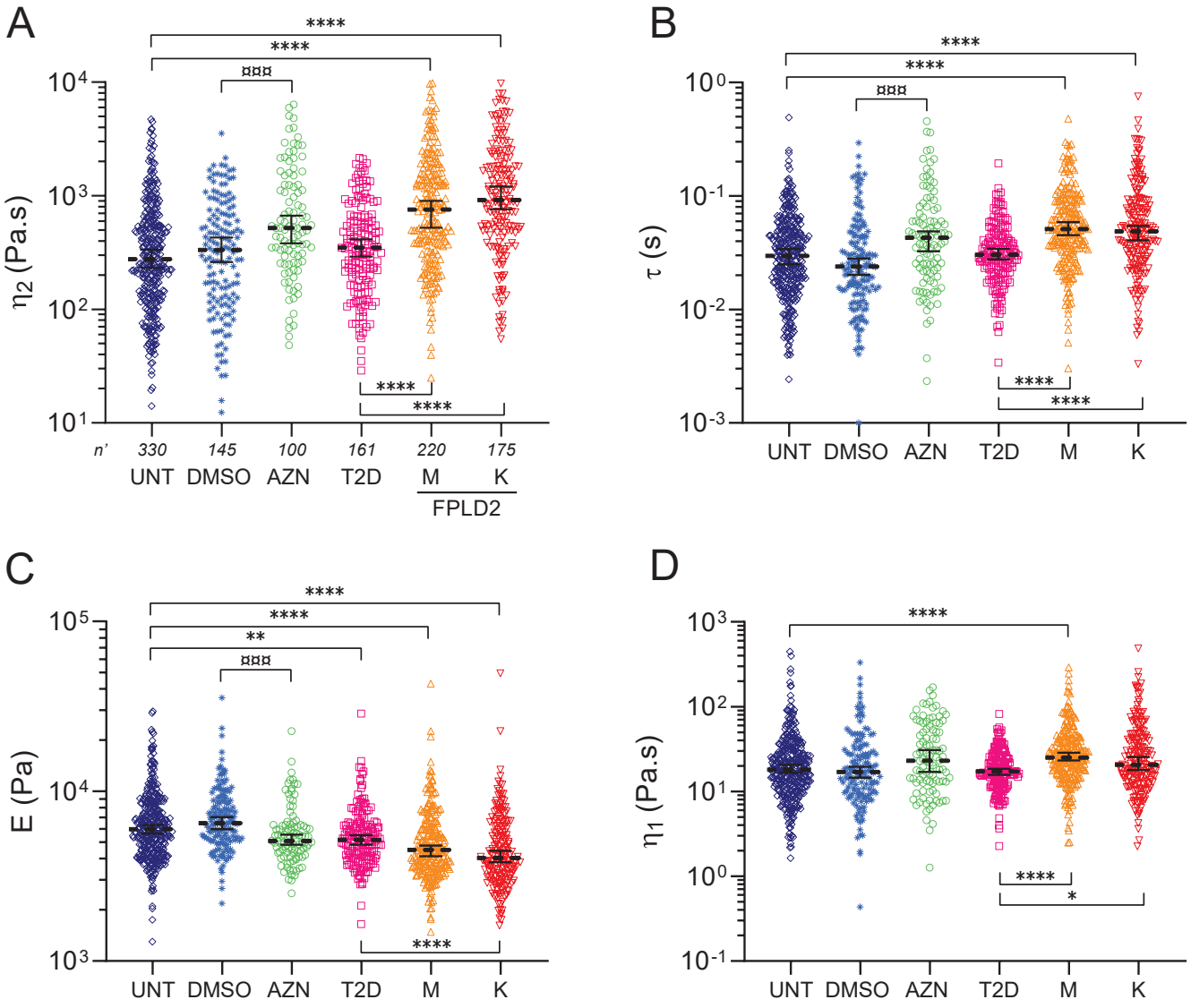

Fig. 5. Dotplot representations of cell viscoelastic parameters extracted with the rheological model. Cells as in Figs. 3, S2 and S3. The plots in A,C-D correspond to the bar plots in Fig. 3D-F and illustrate the number of analyzed cells. A) Long-time viscosity η_2. B) Viscoelastic raising time τ related to short-time elastic modulus E and viscosity η_1 as $\tau = 3\pi\eta_1/E$. C) Elastic modulus E. D) Short-time viscosity η_1. Number of experiments : N $\geq$ 3 ; number of fitted curves: *n'*.

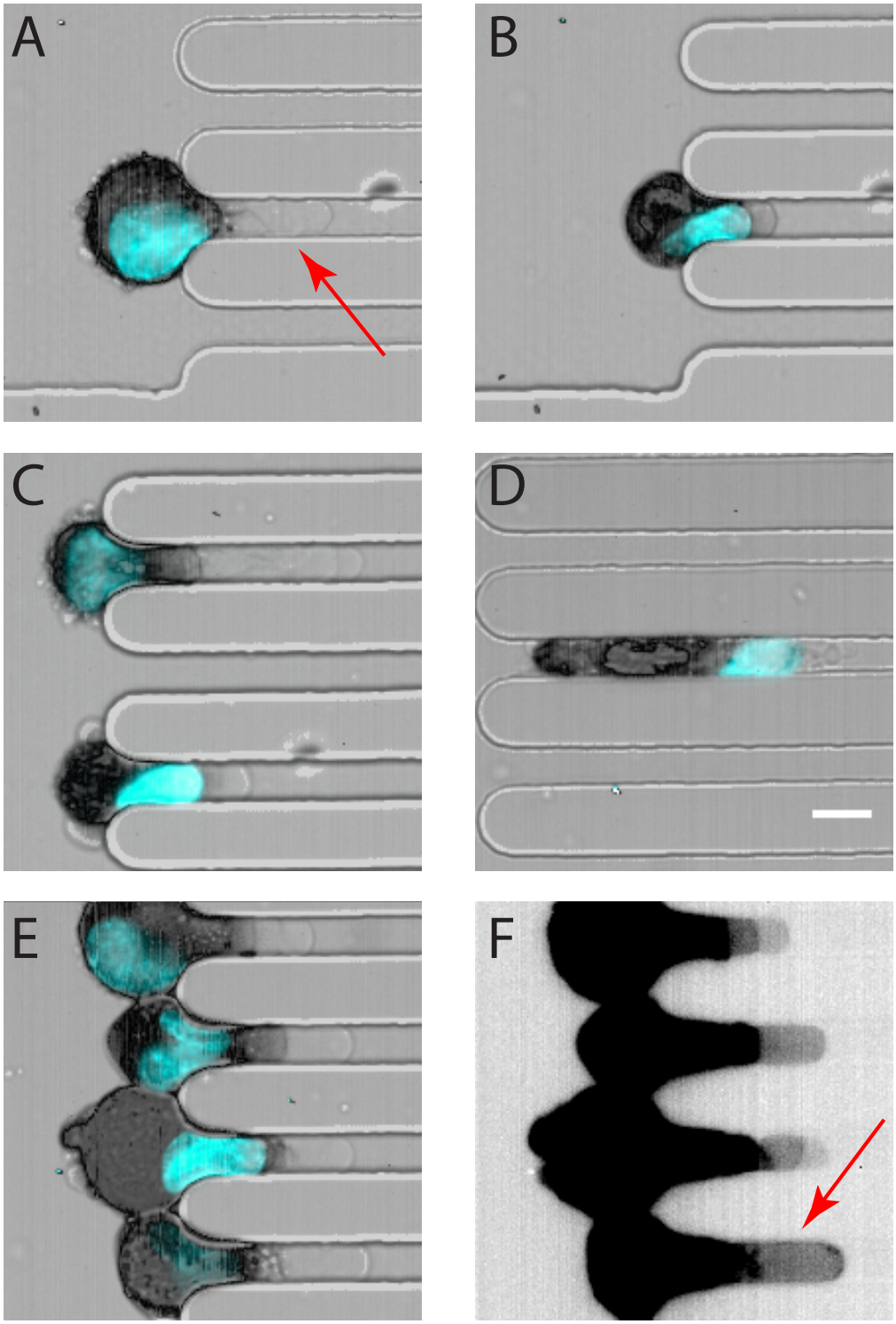

Fig. 6. The cell forms a bleb at the front that precedes the actin cortex and the nucleus during deformation in the constriction. The cell membrane, actin and nucleus are imaged at different timepoints during entry in constriction. A) The cell comes into contact with the constriction and a bleb immediately enters (phase I). B) The bleb moves forward, the actin cortex and the nucleus slowly deform (phase II). C) The nucleus has completely entered the constriction and the rear of the cell deforms (bottom cell), the bleb is still present at the front (phase III). D) The cell is fully deformed and transits through the constriction, with the bleb at the front followed by actin, nucleus and cell rear (phase IV). E-F) Saturating the image highlights the transparent front bleb, with the actin in black. Cell membrane is imaged in brightfield; nucleus and F-actin are imaged in epifluorescence, via Hoechst (blue) and SPY-actin 555 (black) labelling, respectively. Red arrows indicate some blebs. Scale bar = 10 μm.

A

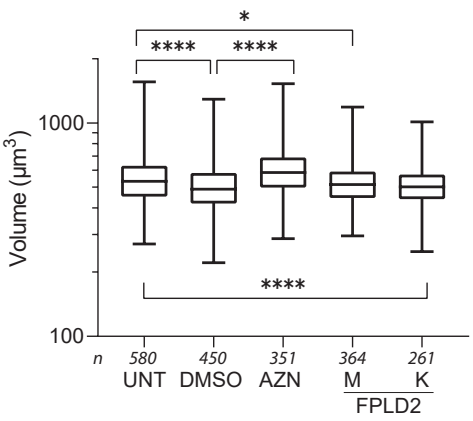

	Nuclear Volume (μm)	
	Median	95% CI
UNT	533	521-549
DMSO	489	477-508
AZN	586	571-605
FPLD2 M	514	502-527
FPLD2 K	502	586-524

B

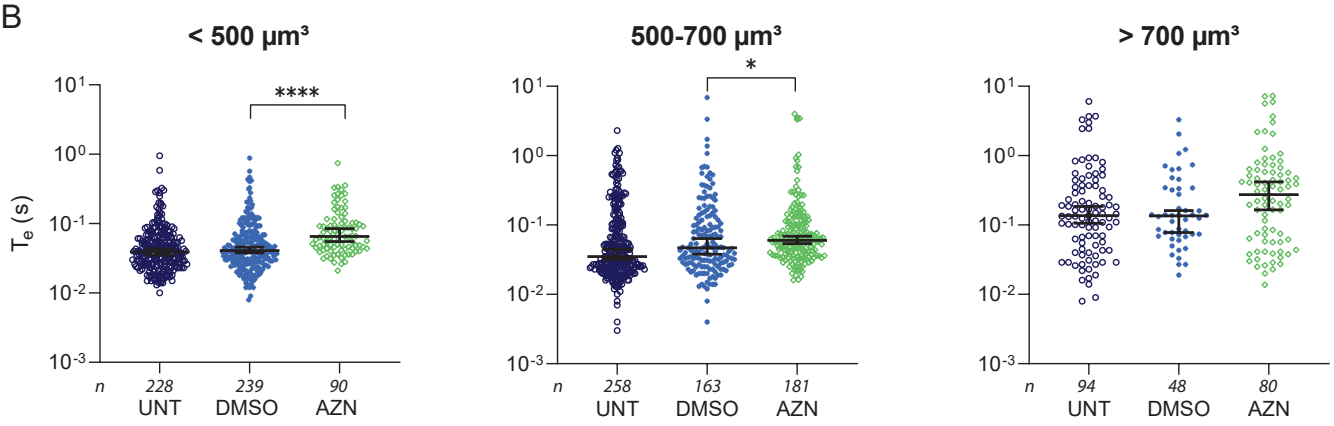

C

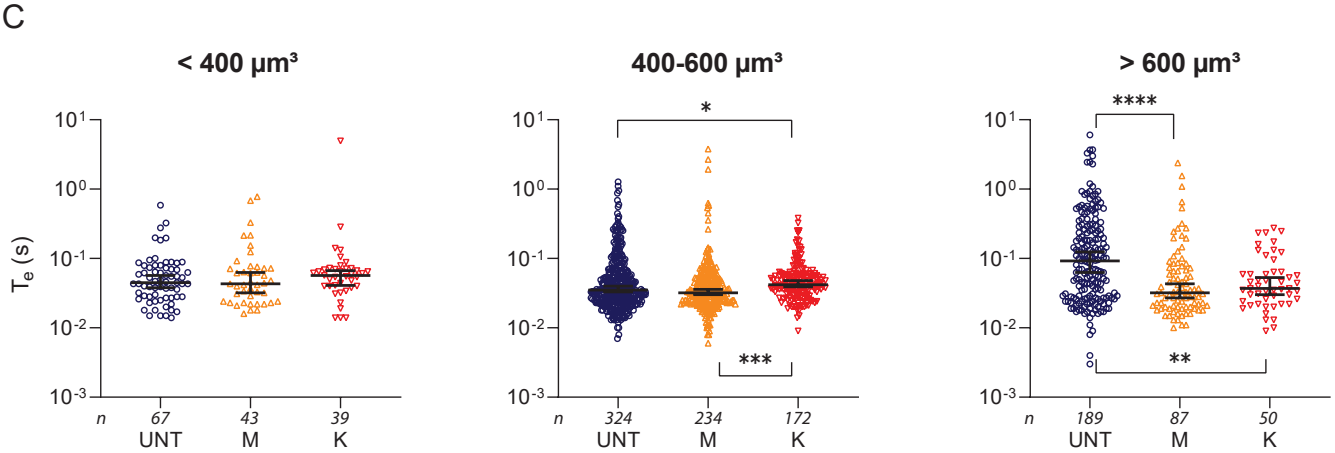

Fig. 7. The entry time of isolated nuclei in constrictions does not correlate with their volumes. A) Volumes of isolated nuclei, computed from microfluidic images. Left: Boxplot representation of the nuclear volume, with median values, 25% and 75% percentiles, and min/max values as whiskers. Right: Table recapitulating median values and 95% CIs. B-C) Dotplot representations of entry times sorted in three size populations that were defined based on the median volumes of nuclei from AZN cells (≈600 μm, B) and from FPLD2 M/K cells (≈500 μm, C). Number of experiments: N $\geq$ 4; number of analyzed nuclei: *n*.

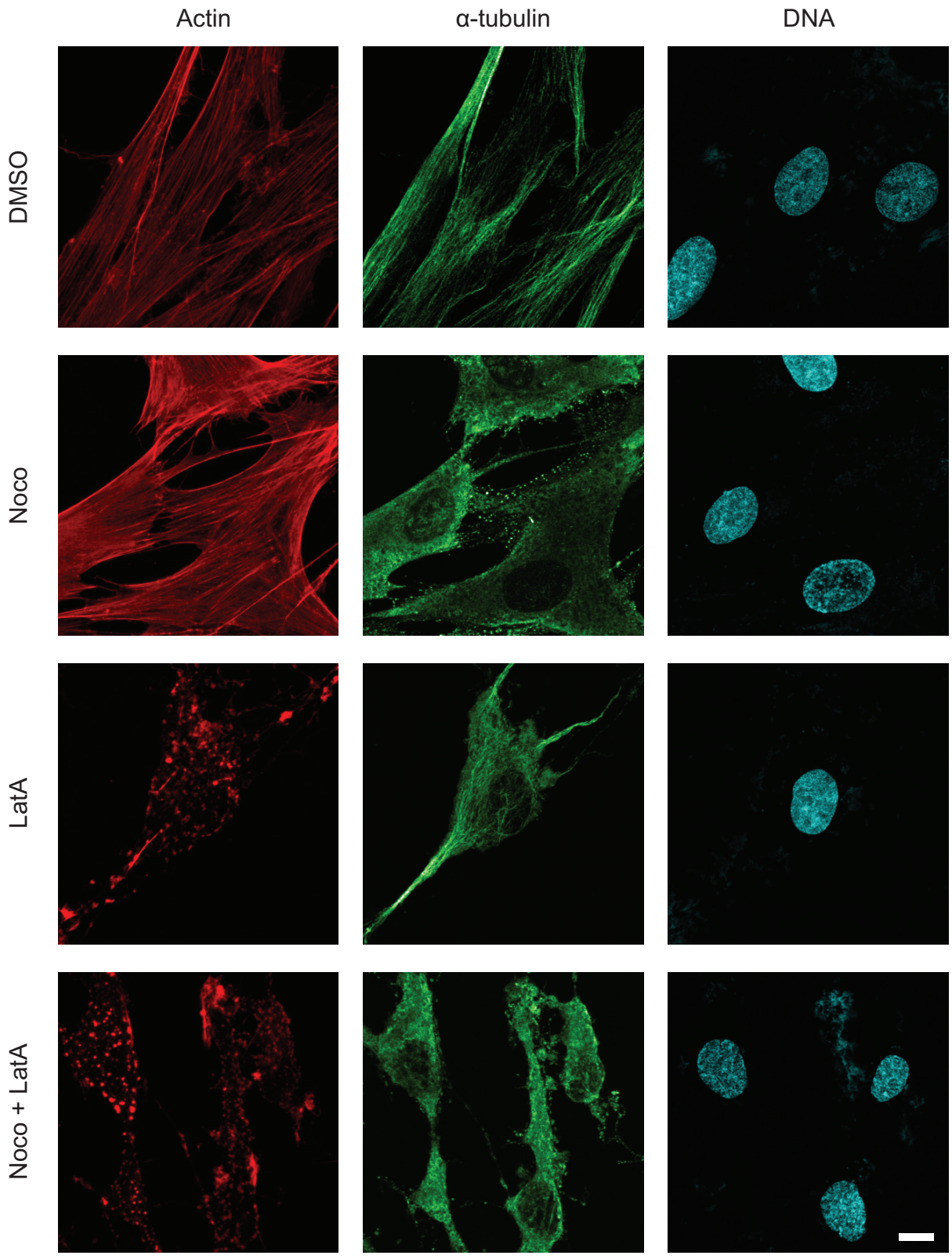

Fig. 8. Actin and microtubule network depolymerization by drug treaments. Maximal intensity projection from confocal z-stacks of F-actin (red), α-tubulin (green) and DNA (blue). Adhered UNT cells were incubated with DMSO, or treated with nocodazole (Noco), latrunculine A (LatA) or both nocodazole and latrunculine A (Noco+Lat A) prior to immunostaining. Scale bar: 10 μm.

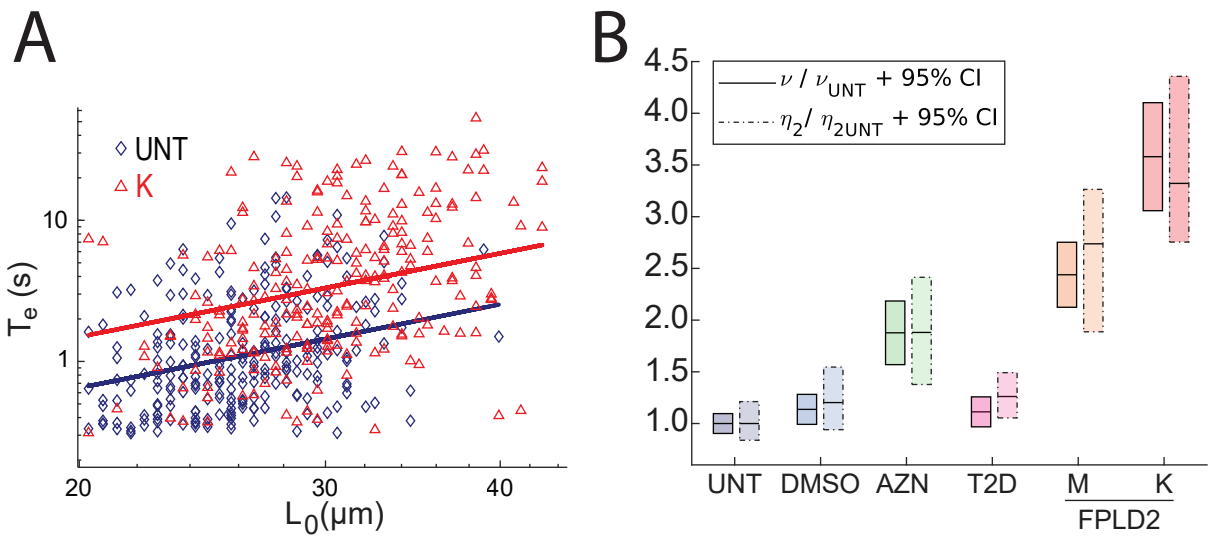

Fig. 9. Alteration of long time viscosity is detected by a simple relationship between entry time and cell initial length. (A) Dependence of the entry time T_e with the cell initial length L_0 for UNT and K cells. Data are plotted in log-log scale and fitted with the scaling law $T_e \sim \nu L_0^2$. Cells with T_e < 0.3 s are not considered. (B) Boxplots of the constant ν extracted from the scaling law fit (solid line) and of long-time viscosity η_2 (dashed line), normalized to the values obtained for UNT cells (median values $\pm$ 95% CIs).

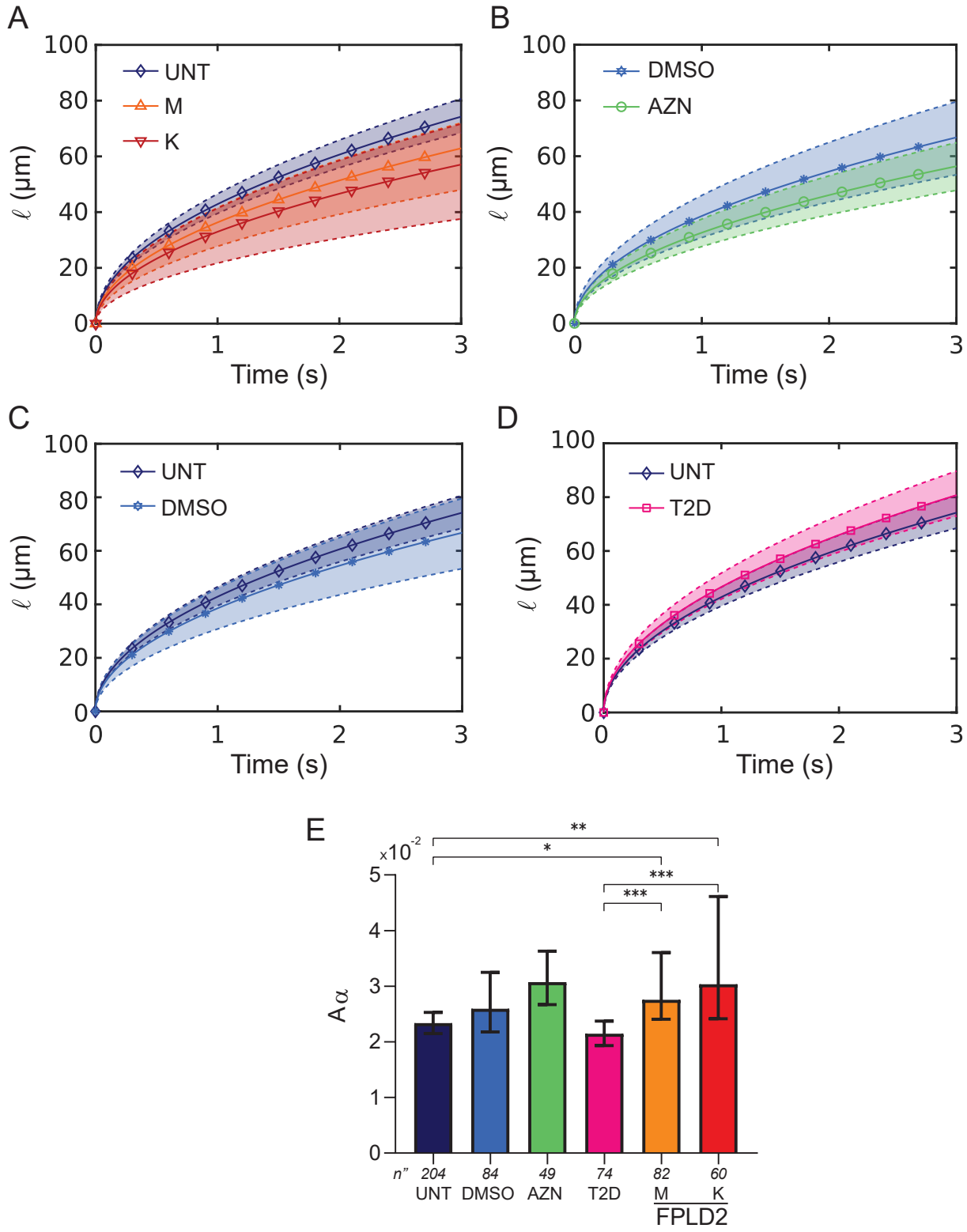

Fig. 10. Tongue length fits using a power law. (A-D) Power law fits $\ell = \ell_0 + t^{0.5}/A_\alpha$ for (A) UNT *vs* M and K cells, (B) DMSO *vs* AZN cells, (C) UNT *vs* DMSO cells, and (D) UNT *vs* L cells. Solid curves and symbols indicate the median fits plotted with the median values of the parameters, dashed upper and lower curves delineate the 95% CIs. (E) Comparison of A_α values extracted from the power law fits for the different cell types (medians $\pm$ 95% CIs). Number of experiments: N $\geq$ 3; number of fitted curves: *n"*.

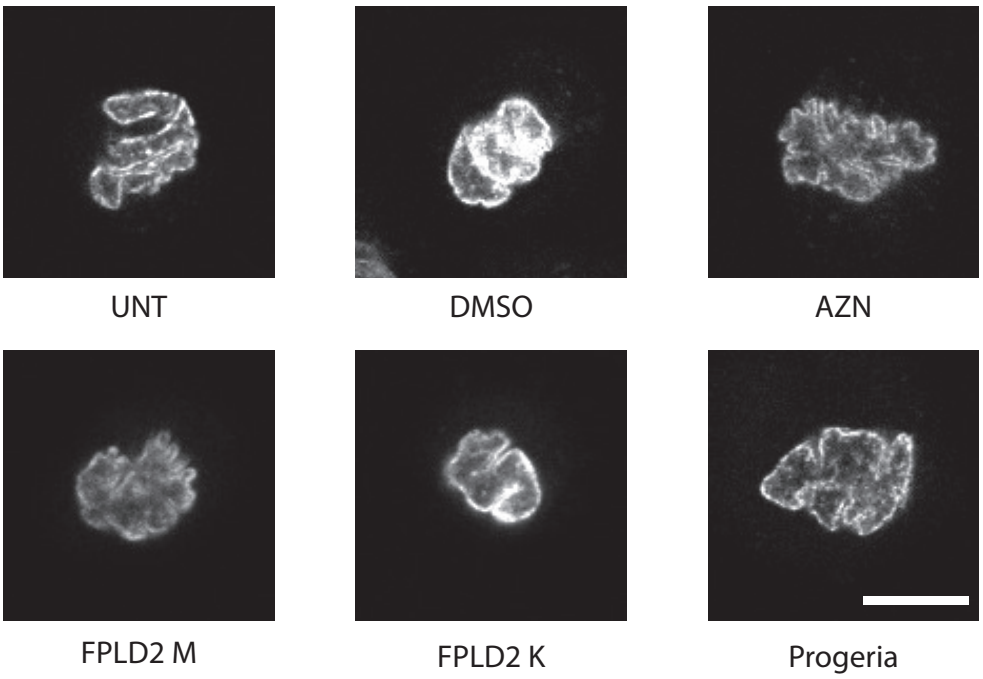

Fig. 11. Nuclei of cells in suspension are wrinkled. UNT: untreated control cells; DMSO: control cells incubated with DMSO for 48 h; AZN: control cells treated with AZN (in DMSO) for 48 h; M,K: cells from patients with FPLD2, Progeria: cells from a patient with HGPS. Typical confocal planes of nuclei labelled with Hoechst. Scale bar: 10 μm.

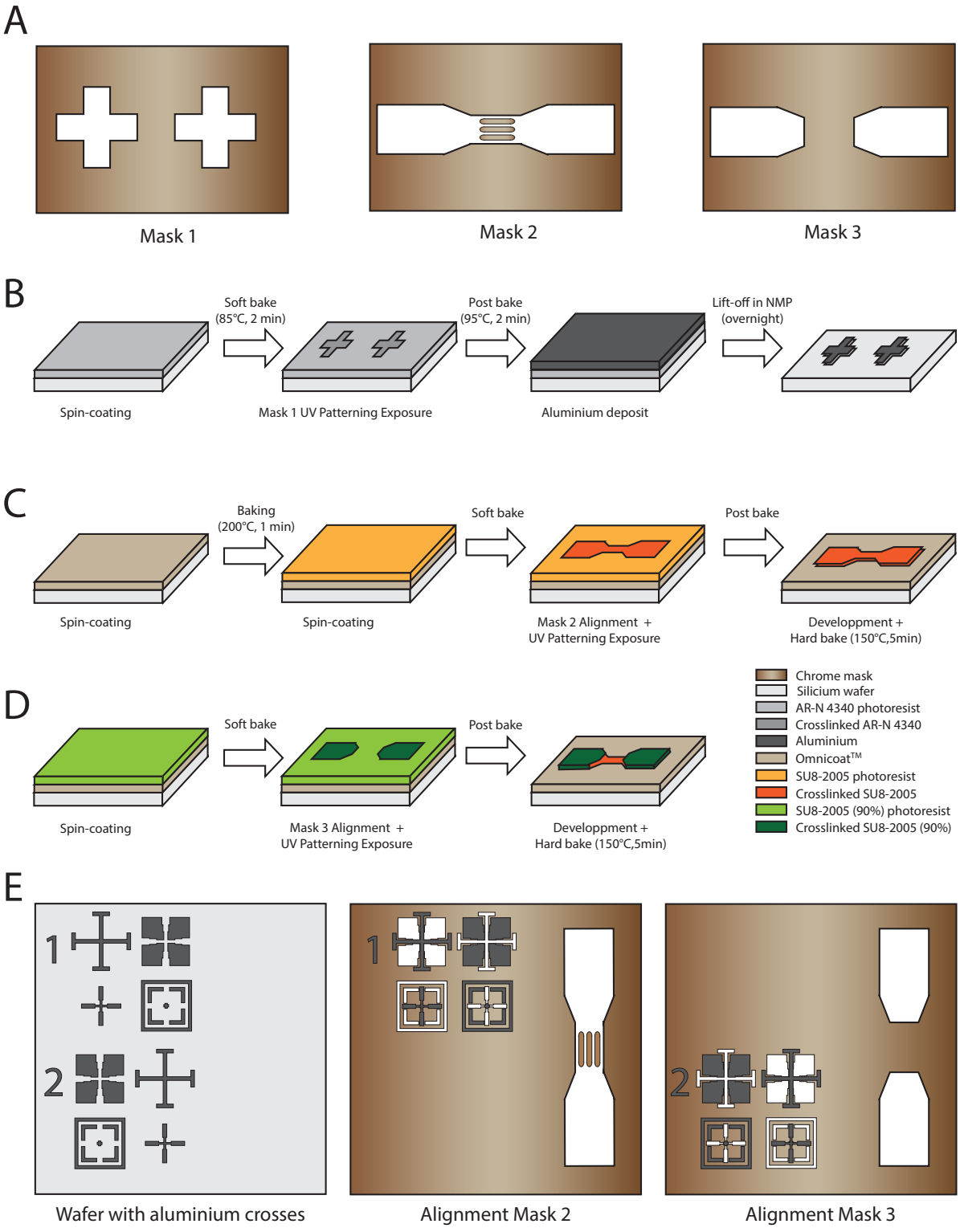

Fig. 12. Workflow of master mold fabrication. A) Simplified schematics of the three masks used to create the mold: Mask 1, alignment crosses; Mask 2, main channel with micrometer-sized constrictions in the central part; and Mask 3, main channel without constrictions. B-D) Steps to create the two-height master mold. E) Alignment of masks 2 and 3 prior to UV patterning exposure.

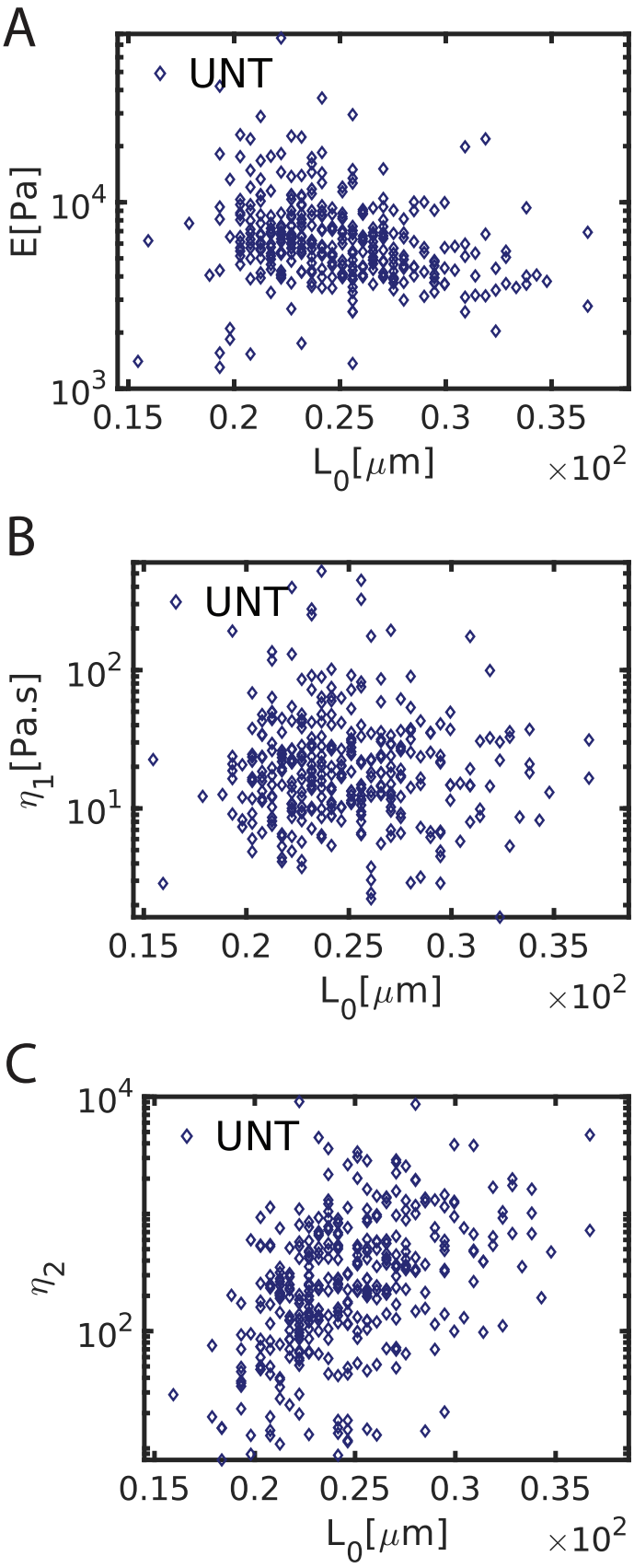

Fig. 13. The viscoelastic parameters are independent of cell size. The effective elastic modulus E and viscosities η_1, η_2 extracted from the fits of tongue length curves of individual cells are plotted as a function of the cell initial diameter L_0. The plots correspond to one data set of untreated cells, and are representative of all cell types and data sets.